

# Computational fluid dynamics-based structure optimization of ultra-high-pressure water-jet nozzle using approximation method

Yuan-Jie Chen<sup>1\*</sup> and Ting Zhou<sup>2</sup>

<sup>1</sup>Institute of Ocean Engineering and Technology, Ocean College, Zhejiang University, Zhoushan, 31602, China

<sup>2</sup>Department of Convergence Study on the Ocean Science and Technology, Korea Maritime and Ocean University, Busan 49112, Republic of Korea

\*Correspondence: chenyj61@zju.edu.cn

This manuscript was compile on January 1, 2025

## Abstract

Since the geometry structure of ultra-high-pressure (UHP) water-jet nozzle is a critical factor to enhance its hydrodynamic performance, it is critical to obtain a suitable geometry for a UHP water jet nozzle. In this study, a CFD-based optimization loop for UHP nozzle structure has been developed by integrating an approximate model to optimize nozzle structure for increasing the radial peak wall shear stress. In order to improve the optimization accuracy of the sparrow search algorithm (SSA), an enhanced version called the Logistic-Tent chaotic sparrow search algorithm (LTC-SSA) is proposed. The LTC-SSA algorithm utilizes the Logistic-Tent Chaotic (LTC) map, which is designed by combining the Logistic and Tent maps. This new approach aims to overcome the shortcoming of 'premature convergence' for the SSA algorithm by increasing the diversity of the sparrow population. In addition, to improve the prediction accuracy of peak wall shear stress, a data prediction method based on LTC-SSA-support vector machine (SVM) is proposed. Herein, LTC-SSA algorithm is used to train the penalty coefficient  $C$  and parameter  $\gamma$  of SVM model. In order to build LTC-SSA-SVM model, optimal Latin hypercube design (Opt LHD) is used to design the sampling nozzle structures, and the peak wall shear stress (objective function) of these nozzle structures are calculated by CFD method. For the purpose of this article, this optimization framework has been employed to optimize original nozzle structure. The results show that the optimization framework developed in this study can be used to optimize nozzle structure with significantly improved its hydrodynamic performance.

**Keywords:** Water jet nozzle, Wall shear stress, Logistic-Tent chaotic (LTC), Sparrow search algorithm (SSA), support vector machine (SVM)

Rho LaTeX Class © This document is licensed under Creative Commons CC BY 4.0.

## 1. Introduction

In recent years, the number of ships has experienced an unprecedented expansion, primarily driven by the rapid development of economic globalization, international trade exchanges, and increasing human activities (Gu, Yu et al. 2020). However, the underwater surface of a ship's hull is prone to biofouling and rust accumulation when it is exposed to water for long periods of time during sailing and docking. Numerous studies have indicated that ship hulls are subject to the detrimental effects of pollutants, resulting in corrosion, heightened surface roughness, diminished speed, escalated fuel consumption, and amplified greenhouse gas emissions (Schultz 2007, Gu, Mou et al. 2015). Governments worldwide are increasingly concerned about environmental and energy consumption issues. In cases where hull deposits and corrosion scale become problematic, their removal becomes crucial.

Ultra-high pressure water jets are an innovative and eco-friendly technology used for surface cleaning. They have been widely adopted for removing rust and marine attachments from hulls. The effectiveness of water jet technology largely depends on the use of UHP water-jet nozzles, which are essential components for practical applications. Thus, finding strategies to improve the performance for UHP water-jet nozzle is critical to enhance the rust-removing efficacy for water jet technology. UHP water-jet nozzles are crucial actuators in generating high-speed water jets. Several studies have confirmed that the ability of a high-speed water jet to remove material from a target surface is directly influenced by the radial peak wall shear stress (Chen and Chen 2022, Huang and Chen 2022). The impinging exfoliation via a UHP water jet imposed on the target surface generally comes into play to remove the corrosion and other residual coatings on the target surface only when the impinging force (composed of wall shear stress and water wedge effect) of the water jet is more significant than a particular threshold value. The radial peak wall shear stress can be used as an indicator for evaluating the hydrodynamic performance of UHP water-jet nozzle, which is difficult to get in advance due to complex experiments and sophisticated test

facilities.

In the twenty-first century, the design of nozzle structures has predominantly relied on simulation-based design (SBD) technique due to the rapid development of CFD and optimization techniques. This technique aims to maximize the peak wall shear stress, thereby enhancing operational efficiency. The CFD tools have become the main method for calculating the peak wall shear stress of the nozzle and simulating the flow field, but its calculation time is rather long. In order to promote the application of SBD technique to the practical engineering, and to reduce the computational time of a typical CFD work, the application of data-driven surrogate model has become the key to the development in nozzle structure optimization. By processing of data-driven surrogate model, the original complex problem is turned into a relatively small approximate subproblem, and the optimal solution of the original problem is obtained by successive approximation. The issue of predictions using the surrogate model has been highlighted by researchers, not only in engineering (Liu, Fan et al. 2015, Wu, Weisbrich et al. 2017, Wang, Wu et al. 2019) but also in other fields (Jin, Olhofer et al. 2001, Feldman, Provan et al. 2010, Dhiman and Toshniwal 2020).

In recent years, machine learning algorithms (MLAs) have been extensively utilized for constructing data-driven surrogate models (e.g., artificial neural network (ANN) and support vector machine (SVM)). These models offer several advantages, such as the ability to handle unlimited input data, fast processing speed, and accurate predictions. By utilizing computer simulations, MLAs have proven to be effective in predicting and analyzing data using techniques such as learning, control, and identification. These algorithms have been successfully applied to various problems (Ghalandari, Ziamolki et al. 2019, Sun, Cao et al. 2019, Weichert, Link et al. 2019). As a family member of MLAs, SVM aims to minimize the sample points by constructing a hyperplane in high dimensional space and exhibits good prediction precision with fewer sample points. There is now much work demonstrating that the SVM has higher predictive precision and convergence rate compared to the backpropagation neural network (BPNN) for data prediction. Wang, Sun et al. (2019) compared the

prediction results of SVM and BPNN for the core deflection during wax injection in investment casting. They found that SVM exhibited stronger adaptation and better generalization ability, allowing for the construction of a more accurate approximate model for core deflection (Wang, Sun et al. 2019, Herulambang, Hamidah et al. 2020). However, there are few literatures have been published for predicting peak wall shear stress using SVM. In the light of these considerations, the SVM has been used into the UHP nozzle structure optimization in this study to approximately calculate the peak wall shear stress values.

SSA is a population-based meta-heuristic algorithm developed by Xue and Shen (2020) to solve continuous optimization problems. It has obtained a lot of interest in diverse optimization problems because of the advantages of fast convergence, high search accuracy and strong robustness (Yang, Li et al. 2021). Although the SSA has become a relative mature method, its main ability to optimize the problem is to rely on the mutual cooperation and mutual influence between sparrow individuals. There is no mutation mechanism for individuals within the population. After finding the optimal solution, other individuals quickly move closer to the optimal solution, making it difficult for the algorithm to effectively control the global exploration and local development process and thus fall into the local optimum, causing the algorithm to converge prematurely. The “premature convergence” of the algorithm is a shortcoming of all swarm intelligence optimization algorithms, and it will also exist in the SSA. Therefore, many researchers have put forward a variety of improvement measures to prove that the new methods are superior to standard SSA algorithm (Arora and Singh 2019, Jianhua and Zhiheng 2021, Ouyang, Qiu et al. 2021). As a new optimization technique, chaos optimization has been widely used in recent years. Chaos mapping has the characteristics of ergodicity and randomness and it can compensate for the shortcomings of SSA algorithm in terms of population diversity. Two of the most commonly used approaches for chaotic mapping are Tent map and Logistic map. However, both of these have a limited range of parameters and a low level of chaos, which can be a disadvantage. To address this issue, a new chaotic map that combines the Logistic and Tent maps was developed. In this paper, an improved SSA (i.e., LTC-SSA) algorithm has been proposed by embedding the LTC map to the SSA algorithm to increase the diversity of the population. The performance of this hybrid algorithm has been evaluated by employing them in the optimization of the 10 benchmark functions. Although SVM has some advantages, there also exist some problems in its application. Due to commonly used SVM theory have been performed mostly using fixed parameter C, and parameter g, it has the lowest predictive accuracy, regardless of the number of bootstrapping times (Wu, Tzeng et al. 2007). By developing the improved SVM (Smits and Jordaan 2002, Gu, Chang et al. 2021, Harimoorthy and Thangavelu 2021), these problems can be overcome effectively. In this article, to improve the accuracy of the peak-wall-shear-stress prediction using SVM, an effective LTC-SSA algorithm developed is used to optimize the parameter C, and parameter g of SVM.

The aim of present work is to describe a practical UHP water-jet nozzle optimization loop using the LTC-SSA-SVM method. In Section 2, an improved LTC-SSA is proposed and its applicability is verified by 10 constraint benchmark functions, and compared with SSA, GWO and PSO algorithms. In Section 3, the efficiency of CFD simulations is validated by comparing them with existing experimental data. This ensures that the CFD method can be used confidently in the subsequent text. In Section 4, The design variables (i.e.,  $a$ ,  $b$ ,  $c$ ,  $d$ , and  $\theta$ ) and their corresponding ranges of values are carefully selected. Subsequently, 150 simulation jobs are generated to create a simulation database using the Opt LHD method. Finally, an enhanced LTC-SSA-SVM model is developed to approximately calculate the peak wall shear stress and its effectiveness is verified by comparing with SVM, BPNN, GBDT and RBFNN. In Section 4, peak wall shear stress

calculated via data-driven surrogate model is selected as the objective function, and the geometric structure of UHP water-jet nozzle is optimized to obtain the optimal solution using an LTC-SSA algorithm. Finally, a summary of key findings and conclusions are presented in Section 6.

## 2. Optimizers

### 2.1. Overview of sparrow search algorithm (SSA)

SSA is a nature-inspired algorithm based on the behavior of sparrows foraging and anti-predation (Xue and Shen 2020). It is worth noting that there are two distinct kinds of sparrows in the population, namely producers who are responsible for searching food, and scroungers who obtains the food discovered by producers. While two above-mentioned roles can be switched via an ingenious strategy, their ratios stay constant in the entire population. Recent literature points that this algorithm has superior search accuracy, convergence speed and stability compared with other state-of-the-art algorithms. The main steps of the algorithm are as follows:

*Step1:* Create and initialize the population. The number of sparrows ( $n_s$ ), producer ratios ( $P_D$ ) and maximum number of iterations ( $M$ ), as well as the alarm value ( $R_2$ ) and safety threshold ( $S_T$ ) are clearly determined at this stage. The initial position of sparrows is written in matrix form as shown in Eq. (1).

$$X = \begin{bmatrix} x_{11} & x_{12} & \cdots & \cdots & x_{1,d} \\ x_{21} & x_{22} & \cdots & \cdots & x_{2,d} \\ \vdots & \vdots & \vdots & \vdots & \vdots \\ x_{n_s,1} & x_{n_s,2} & \cdots & \cdots & x_{n_s,d} \end{bmatrix} \quad (1)$$

where  $d$  is the dimension of the selection variables,  $x_{i,j}$  ( $i = 1, 2, \dots, n_s; j = 1, 2, \dots, d$ ) is the position of the  $i$ th sparrow in the  $j$ -th dimension and  $X$  is the population of candidate solutions. The Fitness values of sparrows can be calculated by using the following Eq. (2). In Eq. (2), the value of each row in  $F_X$  represents the fitness of the  $i$ -th sparrow.

$$F_X = \begin{bmatrix} f [ x_{11} & x_{12} & \cdots & \cdots & x_{1,d} ] \\ f [ x_{21} & x_{22} & \cdots & \cdots & x_{2,d} ] \\ \vdots & \vdots & \vdots & \vdots & \vdots \\ f [ x_{n_s,1} & x_{n_s,2} & \cdots & \cdots & x_{n_s,d} ] \end{bmatrix} \quad (2)$$

*Step2:* Update the location of producers and scroungers. In order to bring the entire population closer to the food source, sparrows with the highest fitness are selected as producers, whereas the remaining sparrow population are taken as scroungers. Below is an updated location for the former using Eq. (3),

$$X_{i,j}^{t+1} = \begin{cases} X_{i,j}^t \times e^{\left(\frac{-t}{\alpha M}\right)} & \text{if } R_2 < S_T \\ X_{i,j}^t + QLifR_2 & \geq S_T \end{cases} \quad (3)$$

where  $X_{i,j}^t$  is the current position of the  $i$ -th sparrow in the  $j$ -th dimension at generation  $t$ ,  $\alpha$  is a random number between 0 and 1,  $Q$  is the standard normal distribution random number, and  $L$  denotes a  $1 \times d$  matrix in which all elements are one. if  $R_2 < S_T$ , producers can globally forage without suffering from predators. When  $R_2 \geq S_T$ , predators are detected by some sparrows and all sparrows must rapidly spread to other safe areas.

Rules 3 and 4 must be observed in the case of producers. As mentioned above, certain scroungers monitor the majority of producers. When a producer finds a palatable cuisine, scroungers will leave their current location to fight for it; if they succeed, they can dine immediately; otherwise, Rule 4 will take effect. The relevant position transformation for the scroungers is depicted in Eq. (4),

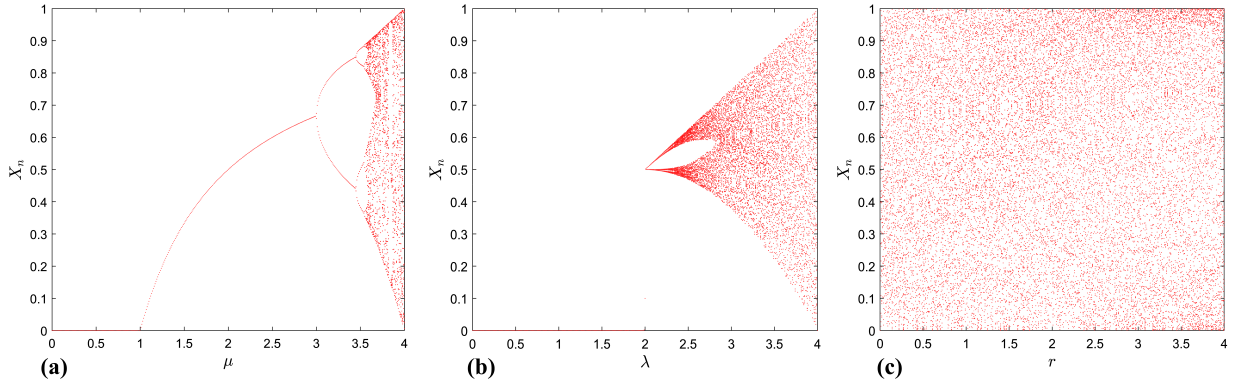


**Figure 1.** The sequence statistical histogram of the (a) Logistic map; (b) Tent map; (c) LTS.

$$X_{i,j}^{t+1} = \begin{cases} Qe^{\left(\frac{X_{i,j}^t - X_{worst}^t}{i^2}\right)} & \text{if } f_i < \frac{n}{2} \\ X_{i,j}^{t+1} + \left| X_{i,j}^t - X_p^{t+1} \right| LA^+ & \text{otherwise} \end{cases} \quad (4)$$

where  $X_p^{t+1}$  is the optimal position of the  $(t+1)$ -th generation of sparrow population, with the worst position at  $t$ -th,  $A$  is a column vector of the same dimension as the individual sparrow, in which internal elements are randomly assigned to 1 or -1, and  $A^+ = A^T(AA^T)^{-1}$ . If  $i \leq \frac{n}{2}$ , the scroungers will actively follow the producers toward the better foraging position. Otherwise, they will combine the exp function property to get rid of the current poorer one.

**Step3:** Select the guards and renew their locations. Following completion of the preceding stages, a selection of sparrows is chosen to serve as scouts in charge of detection and alerting. These sparrows are generally considered to account for 10% to 20% of the whole population, and their status is expressed via the equation. (5).

$$X_{i,j}^{t+1} = \begin{cases} X_{best}^t + \beta \left| X_{i,j}^t - X_{best}^t \right| & \text{if } f_i > f_g \\ X_{i,j}^t + K \left( \frac{\left| X_{i,j}^t - X_{worst}^t \right|}{(f_i - f_w) + \epsilon} \right) & \text{if } f_i = f_g \end{cases} \quad (5)$$

where  $X_{best}^t$  is the current globally optimal location,  $\beta$  is a parameter for controlling step size,  $K$  is a random number between -1 and 1, which describes the sparrow movement,  $f_i$  is the current fitness value of individuals,  $f_g$  and  $f_w$  are the current global best and worst fitness values respectively and  $\epsilon$  is a smallest constant to avoid a zero denominator. If  $f_i > f_g$ , it means that the sparrow is at the edge of the group and vulnerable to predators. When  $f_i = f_g$ , sparrows in the middle of the population are aware of the danger and must therefore move closer to other sparrows to lessen the likelihood of being preyed upon.

**Step 4:** Store location and compare. The current position of each individual is compared with the last iteration. If the new location is better than before, update it and save the best position. In some cases, sparrows may improve their fitness after following the last two steps.

**Step 5:** Check for termination condition. Continually iterate through the above steps until  $t = M$ , if not, stop the algorithm.

## 2.2. Chaotic system

In this section, we use chaotic systems to improve the performance of the SSA algorithm. However, chaotic systems have a limited range of parameters and a low level of chaos, which can be a disadvantage. To address this, we propose a new chaotic system that combines the Logistic and Tent maps. This improved chaotic system is better suited for use with the SSA algorithm.

### 2.2.1. Definition of LTS

Chaos is a common and complex occurrence in nature that can be used to solve search problems. It is useful because it has properties

that make it ideal for searching, including randomness, the ability to be easily traversed, and some regularity. In addition to maintaining a diverse population, chaos can also help algorithms avoid getting stuck at local optima and improve their ability to search globally. The Logistic map is a classic example of a chaotic system that is one-dimensional (1D). It is described by the following equation:

$$Z_{n+1} = \mu Z_n (1 - Z_n) \quad (6)$$

where is  $Z_n$  the  $n$ th chaotic number,  $n$  denotes the number of iterations and  $\mu$  is the control parameter,  $\mu \in (0, 4]$ .

The simple equation mentioned earlier is capable of producing complex and seemingly random behavior. By changing the value of the parameter  $\mu$ , we can generate different chaotic sequences. Figure 1a shows the results of simulating this equation with different values of  $\mu$  using a bifurcation diagram. According to the simulation results, the system is able to exhibit chaotic behavior for a range of values for the parameter  $\mu$ . Specifically, when  $\mu$  is between 3.57 and 4, the system is in a completely chaotic state. This shows the sensitivity of the system to small changes in  $\mu$ , which can result in significant changes in its behavior.

The Tent map is a 1D chaotic system that is piecewise linear. It is similar to the Logistic map in that it exhibits specific chaotic behavior. It is defined by the following equation:

$$Z_{n+1} = \begin{cases} \lambda Z_n / 2, Z_n < 0.5 \\ \lambda(1 - Z_n) / 2, Z_n \geq 0.5 \end{cases} \quad (7)$$

where  $\lambda$  is the control parameter,  $0 < \lambda \leq 4$ . The bifurcation diagram in Figure 1b shows the chaotic sequences generated by the Tent map for different values of  $\lambda$ . It can be seen that when  $\lambda$  is between 2.89 and 4, the system is in a fully chaotic state.

The Logistic map and the Tent map are both chaotic systems, but they have some limitations. They can produce chaotic sequences that are unevenly distributed and have a limited range of chaotic behaviour. In this paper, a new chaotic system called the Logistic-Tent system (LTS) is introduced to address these issues. LTS combines the Logistic map and the Tent map and is defined by the following equation (Zhou, Bao, &Chen, 2014):

$$Z_{n+1} = \begin{cases} \text{mod}((rZ_n(1 - Z_n) + (4 - r)Z_n/2), 1), Z_n < 0.5 \\ \text{mod}((rZ_n(1 - Z_n) + (4 - r)(1 - Z_n)/2), 1), Z_n \geq 0.5 \end{cases} \quad (8)$$

where  $r$  is the control parameter,  $0 < r \leq 4$ . As shown in Figure 1c, the chaotic range for this system, which is based on the Logistic and Tent maps, is also  $(0, 4]$ . This range is much wider than that of the Logistic or Tent map alone.

To confirm that the output sequence of the LTS-based chaotic system is evenly distributed, we performed a statistical analysis using 20,000 randomly chosen points from chaotic sequences generated

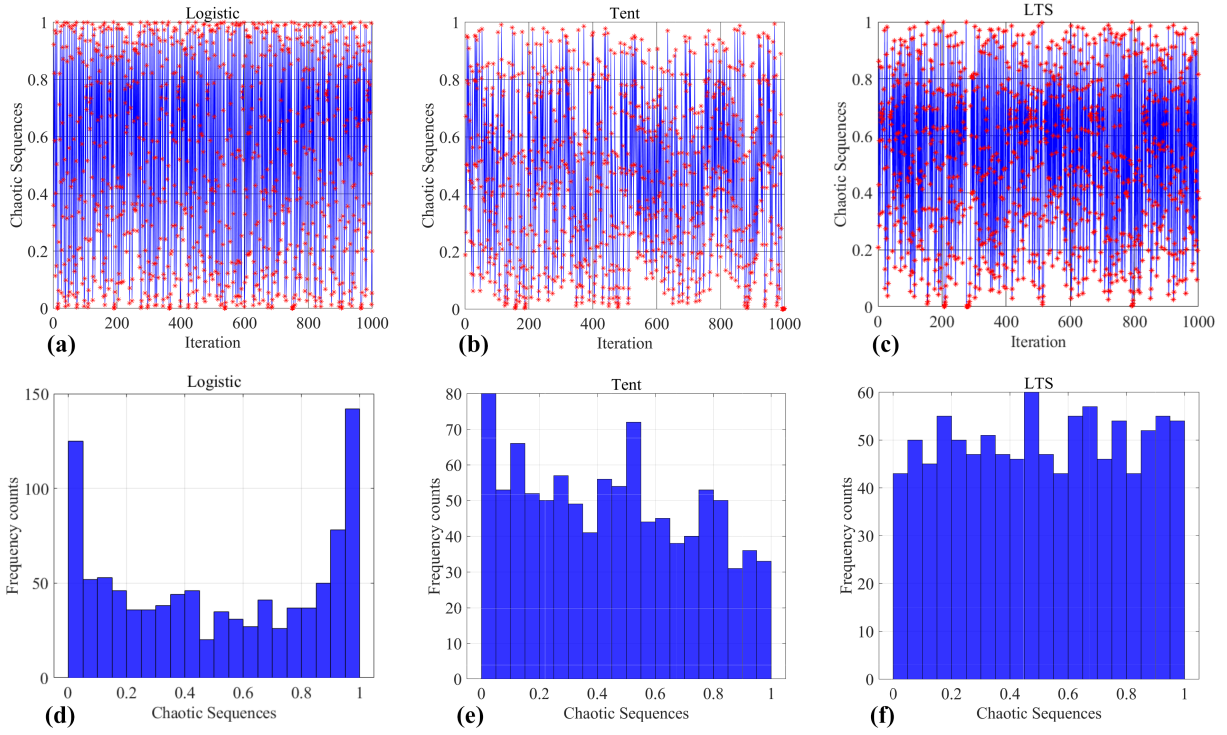


**Figure 2.** The sequence statistical histogram of the (a) Logistic map; (b) Tent map; (c) LTS.

by the Logistic, Tent, and LTS-based systems, as shown in Figure 2a-c. The resulting histograms, shown in Figure 2d-f, indicate that the chaotic sequences generated by the Logistic and Tent maps are unevenly distributed, with most of the points concentrated on either end or in the middle. In contrast, the output sequence of the LTS-based system is evenly distributed across the interval (0, 1).

### 2.2.2. Lyapunov exponent

Lyapunov exponents (LE) are a measure of how sensitive a chaotic system is to changes in its initial conditions (Liu, Sun et al. 2016). If the LE value is greater than 0, the system is considered to be in a chaotic state. The higher the LE value, the more sensitive the chaotic system is to the initial value, which can improve its performance. The LE is calculated using the following equation:

$$LE = \lim_{n \rightarrow \infty} \frac{1}{n} \sum_{i=1}^{n-1} \ln \left| \frac{df(x_i)}{dx_i} \right| \quad (9)$$

Figure 3 shows the LE curves for several chaotic systems, including the Logistic, Tent, LTS, and Double-Sine maps. For simplicity, the control parameter is referred to as  $r$  in this study. The Double-Sine map is an improved version of a widely used chaotic system proposed by Zhou, Hua et al. (2014). The LTS has a much larger LE value and a wider range of control parameters compared to the classic maps and the improved map. Therefore, we use the LTS to improve the performance of the SSA algorithm.

### 2.2.3. LTS chaotic perturbation

In order to avoid the algorithm from converging on local optima, the chaotic perturbation is introduced to the LTC-SSA algorithm to enhance its global search capability and optimization precision. The steps of the chaotic perturbation are described below:

*Step1:* The chaotic variable  $Z_d$  is generated using Eq. (8).

*Step2:* The chaotic variable is introduced into the solution space of the optimization problem according to Eq. (10),

$$X_{new}^d = d_{min} + (d_{max} - d_{min})Z_d \quad (10)$$

where  $d_{min}$  and  $d_{max}$  are the minimum and maximum values of the

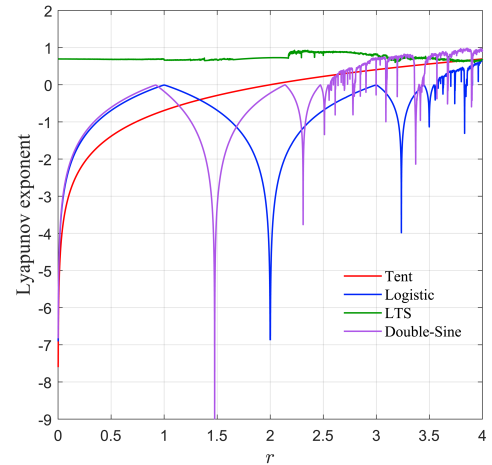


**Figure 3.** Lyapunov exponent.

$d$ -th variable, respectively.

*Step3:* Chaotic perturbation of individuals is performed according to Eq. (11).

$$X'_{new} = (X' + X_{new})/2 \quad (11)$$

where  $X_{new}$  is the amount of perturbation produced by chaos.  $X'$  is an individual that needs chaotic perturbation.  $X'_{new}$  is an individual after chaotic perturbation.

## 2.3. The proposed Logistic-Tent Chaotic sparrow search algorithm

Although SSA algorithm has a good convergence rate, it may not always perform well in finding global optima, which can impact the convergence rate of the algorithm. Therefore, the LTC-SSA algorithm is developed to improve the efficiency of SSA by introducing chaotic perturbation into the algorithm itself, which helps reduce its impact on the convergence rate. Chaos is a type of random-like behaviour that occurs in non-linear, dynamic systems. It is deterministic and characterized by non-periodic, non-converging behaviour



```

for i = (pNum + 1) : pop
    A = floor(rand(1, dim) * 2) * 2 - 1;
    if i > (pop / 2) % Starving followers (
exploration)
        x(sortIndex(i), :) = randn(1) * exp
((worse - pX(sortIndex(i), :)) / (i^2));
        else % Follow the best producer
            x(sortIndex(i), :) = bestXX + abs(pX
(sortIndex(i), :) - bestXX) * (A' * (A * A')
^(-1)) * ones(1, dim);
        end
        x(sortIndex(i), :) = Bounds(x(sortIndex(i),
:), lb, ub);
        fit(sortIndex(i)) = fobj(x(sortIndex(i),
:));
    end

% Update positions of sparrows aware of
danger
c = randperm(numel(sortIndex));
b = sortIndex(c(1:round(pop * 0.2)));
for j = 1 : length(b)
    if pFit(sortIndex(b(j))) > fMin % Outer
sparrows move closer to safety
        x(sortIndex(b(j)), :) = bestX +
randn(1, dim) .* abs(pX(sortIndex(b(j)), :)
- bestX);
    else % Center sparrows move randomly
        x(sortIndex(b(j)), :) = pX(sortIndex
(b(j)), :) + (2 * rand(1) - 1) * abs(pX(
sortIndex(b(j)), :) - worse) / (pFit(
sortIndex(b(j))) - fmax + 1e-50);
    end
    x(sortIndex(b(j)), :) = Bounds(x(
sortIndex(b(j)), :), lb, ub);
    fit(sortIndex(b(j))) = fobj(x(sortIndex(
b(j)), :));
end

% Update personal and global best positions
for i = 1 : pop
    if fit(i) < pFit(i)
        pFit(i) = fit(i);
        pX(i,:) = x(i,:);
    end
    if pFit(i) < fMin
        fMin = pFit(i);
        bestX = pX(i,:);
    end
end
Convergence_curve(t) = fMin;
end

```

Code 1. Matlab Code of the proposed LTSCSSA algorithm.

## 2.4. Validation for LTC-SSA model

### 2.4.1. Parameter setting

The effectiveness of the LTC-SSA algorithm is evaluated using ten benchmark functions including Unimodal and Multimodal as detailed in Table 1. The population size for sparrows is set at 100, and 500 iterations are performed for each function. To ensure the reliability of the results, 50 Monte Carlo runs are conducted for each benchmark function. This allows for a thorough assessment of the LTC-SSA algorithm's performance. The proposed algorithm is also compared with several other optimization algorithms, including SSA, GWO (Yang, 2012), and PSO (Kennedy, 2011), for validation on the benchmark functions. The parameters for these algorithms are presented in Table 2.

### 2.4.2. Validation results

In this section, we choose the optimal value, mean value and the standard deviation of the 10 benchmark functions as the basic criteria. These represent the optimization capability, stability, and robustness of the algorithms, respectively. Table 3 shows the results of LTC-SSA and other algorithms based on the constrained benchmark functions.

For clarity, the optimal data for each group is marked in bold.

Compared with the other algorithms, the LTC-SSA algorithm achieves the closest results to the optimal values of each benchmark function, outperforming the original SSA algorithm in all three metrics, indicating that LTC-SSA has an enhanced ability of finding optimal solutions. It can be inferred from the relatively low mean and standard deviation of the LTC-SSA algorithm that the final output is likely to be stable and not subject to significant fluctuations over time, robustly proving the excellent stability of the algorithm. The results have also shown the significant improvement of the proposed LTC-SSA algorithm with the application of Logistic-Tent chaos instead of the initial algorithm.

In order to further evaluate the performance of the four algorithms on a constrained set of functions, a non-parametric test called Wilcoxon signed is used in this paper, as shown in Table 4.

## 3. Calculation of wall shear stress based on CFD

### 3.1. Geometric modeling

The straight cone convergent nozzle is extensively used in firefighting, hydraulic coal mining, and other industrial fields as a high-efficiency nozzle with good jet performance (Li et al., 2010; Wen et al., 2016). Because almost all of the straight cone convergent nozzles have a distinct character, i.e., concentrated velocity distribution, its hydrodynamic characteristics are commonly superior to other types of nozzles. Moreover, this kind of nozzle can be used under ultra-high injection pressure up to 300 MPa, which is suitable for ship rust removal operations. To obtain the optimal hydrodynamic performance, the straight cone convergent nozzle is used in this study. A 3D parameterized model is established to express variables of the model structure. Figure 5 shows the geometry of straight cone convergent nozzle. The access section length ( $a$ ) is 2 mm, the contraction section length ( $b$ ) is 5 mm, the exit section length ( $c$ ) is 2.5 mm, the outlet radius ( $d$ ) is 0.4 mm, the contraction angle is 22.5 degrees.

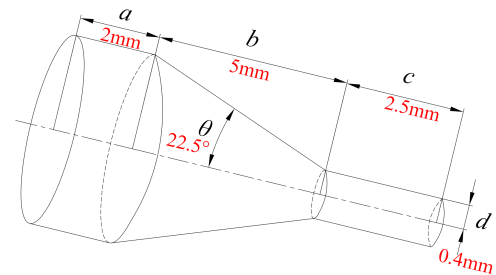


Figure 5. The dimensions of the straight cone convergent nozzle.

### 3.2. Computational domain

Liu et al. (2021) simulated the performance of a 3D impinging jet nozzle using CFD methods. The results demonstrate that the axisymmetric 3D model can accurately describe the flow field features of actual situation. The cylindrical symmetric nozzle, found by Chin et al. (2013), may utilize the symmetry of flow problem, requiring just half of the fluid domain to be modeled, and their simulation results match well with experimental results. Therefore, half of the fluid field can enhance calculation efficiency instead of using the entire fluid field for the simulation of a cylindrical symmetric nozzle. Half of the 3D model is chosen as the study objective in this paper, since the straight cone convergent nozzle is also characterized by a cylindrical

**Table 1.** Details of constrained benchmark functions

Problem	Objective Function	Bound (L, U)	Optimal Value	$n$
$G_1$	$f(x) = \sum_{i=1}^n x_i^2$	(-100, 100)	0	30
$G_2$	$f(x) = \sum_{i=1}^n  x_i  + \prod_{i=1}^n  x_i $	(-10, 10)	0	30
$G_3$	$f(x) = \sum_{i=1}^n \left( \sum_{j=1}^i x_j \right)^2$	(-100, 100)	0	30
$G_4$	$f(x) = \max\{ x_i , 1 \leq i \leq n\}$	(-100, 100)	0	30
$G_5$	$f(x) = \sum_{i=1}^{n-1} [100(x_{i+1} - x_i^2)^2 + (x_i - 1)^2]$	(-30, 30)	0	30
$G_6$	$f(x) = \sum_{i=1}^n  x_i + 0.5 ^2$	(-100, 100)	0	30
$G_7$	$f(x) = \sum_{i=1}^n ix_i^4 + \text{random}[0, 1)$	(-1.28, 1.28)	0	30
$G_8$	$f(x) = \sum_{i=1}^n -x_i \sin(\sqrt{ x_i })$	(-500, 500)	-12569.5	30
$G_9$	$f(x) = \sum_{i=1}^n (x_i^2 - 10 \cos(2\pi x_i)) + 10n$	(-5.12, 5.12)	0	30
$G_{10}$	$f(x) = \frac{1}{4000} \sum_{i=1}^n (x_i^2) - \prod_{i=1}^n \cos\left(\frac{x_i}{\sqrt{i}}\right) + 1$	(-600, 600)	0	30

**Table 2.** Key parameters for four algorithms.

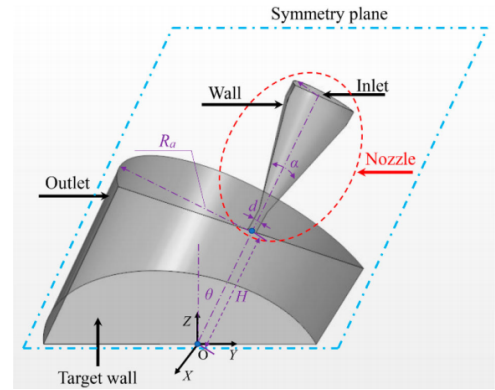
Algorithm	Parameters
LTC-SSA	$P_D = 0.2, n_s = 100, S_T = 0.8, M = 500$
SSA	$P_D = 0.2, n_s = 100, S_T = 0.8, M = 500$
PSO	$C_1 = 1.49, C_2 = 1.49, \omega = 0.729, M = 500$
GWO	$\alpha$ decreases linearly from 2 to 0, $0 \leq r_1 \leq 1, 0 \leq r_2 \leq 1$

axisymmetric feature. The computation domain comprises fluid volume inside the nozzle's internal chamber and fluid volume between the water jet outlet and target wall surface. Figure 6 shows a 3D depiction of the computational domain, where  $R_a$  is the radius of the outer cylindrical computational domain. The static pressure inlet boundary condition is imposed on the cross-section (perpendicular to central axis of water jet) of the access section (a). Water jet from the nozzle impinges the target wall, spreads, reflects and ultimately splashes, leaving the domain via the cylindrical pressure outlet boundary condition. According to the numerical simulation setup performed by Jaramillo et al. (2012),  $R_a$  should be large enough to illustrate the impinging details after the water jet impacts on the target wall. Under this criterion, the  $R_a$  was set to be  $60d$  (i.e.  $R_a = 12\text{mm}$ ), which can sufficiently satisfy the requirement of capturing more details related to water jet and splashing droplets.

### 3.3. Calculation methods

#### 3.3.1. Multiphase model

The CFD method is the most common way to calculate the wall shear stress, particularly in the cases related to UHP impinging water jet, instead of experiments. The UHP impinging water jet is a turbulent flow in the liquid-vapor-gas three-phase flow field (Xiao et al., 2020). The multiphase volume of fluid (VOF) model available in STAR-CCM+ is chosen to effectively simulate the flows inside the nozzle chamber. The VOF model can predict the interface shape of two or more immiscible fluids (Xiao et al., 2020). The concept of volume fraction related to each phase is introduced in this model and the interface shape can be obtained by calculating the volume fraction of the phases in each control volume. All multi-phase components at any given position have the same velocity and pressure.

**Figure 6.** The dimensions of the straight cone convergent nozzle.

In the computational domain, the equations regulating continuity and momentum are as follows (Cebeci & Bradshaw, 1977):

$$\frac{\partial \rho}{\partial t} + \nabla \cdot (\rho U) = 0 \quad (12)$$

$$\frac{\partial \rho U}{\partial t} + \nabla \cdot (\rho U U) = -\nabla P + \nabla \cdot \sigma \quad (13)$$

The phase transfer equations of the three phases are listed as follows:

$$\frac{\partial \alpha_v \rho_v}{\partial t} + \nabla \cdot (\alpha_v \rho_v U) = \dot{R}_e - \dot{R}_c \quad (14)$$

$$\frac{\partial \alpha_i \rho_i}{\partial t} + \nabla \cdot (\alpha_i \rho_i U) = 0 \quad (15)$$

$$\alpha_i + \alpha_v + \alpha_l = 1 \quad (16)$$

where  $\dot{R}_e$  and  $\dot{R}_c$  are the phase transition mass transfer rates between the vapor and liquid phases, respectively. The volume fractions of the liquid, vapor, and air phases are represented by  $\alpha_l$ ,  $\alpha_v$ , and  $\alpha_i$  respectively. The Rayleigh-Plesset equations are utilized to establish the transport relationship between the liquid and vapor phases in the current mainstream cavitation model (Zhang, Dou et al. 2021). A homogeneous equilibrium model based on barotropic fluids is an option for addressing the phase shift of liquid to the liquid-vapor

**Table 3.** The performance test results of four different algorithms on 10 benchmark functions.

Type	Problem	LTC-SSA	SSA	PSO	GWO
Optimal value	$G_1$	<b>0.00e+00</b>	<b>0.00e+00</b>	6.51e-16	4.46e-35
	$G_2$	<b>0.00e+00</b>	1.14e-317	2.81e-19	2.18e-20
	$G_3$	<b>0.00e+00</b>	<b>0.00e+00</b>	9.51e-11	3.33e-11
	$G_4$	<b>0.00e+00</b>	<b>0.00e+00</b>	2.23e-02	3.93e-09
	$G_5$	<b>8.79e-11</b>	5.12e-09	2.49e+00	2.59e+01
	$G_6$	<b>2.43e-24</b>	4.19e-12	6.06e-16	4.43e-05
	$G_7$	<b>2.12e-05</b>	4.09e-05	1.33e-03	2.89e-04
	$G_8$	<b>1.28e+04</b>	-8.95e+03	2.42e+03	4.64e+03
	$G_9$	<b>0.00e+00</b>	<b>0.00e+00</b>	3.97e+00	5.68e-14
	$G_{10}$	<b>0.00e+00</b>	<b>0.00e+00</b>	2.33e+00	0.00e+00
Mean value	$G_1$	<b>3.18e-169</b>	1.03e-165	7.17e-08	6.47e-33
	$G_2$	<b>6.84e-101</b>	1.59e-92	2.89e-18	6.63e-20
	$G_3$	<b>2.96e-126</b>	1.89e-121	3.21e-04	2.17e-08
	$G_4$	<b>7.04e-93</b>	5.97e-87	1.54e-01	2.45e-08
	$G_5$	<b>9.97e-08</b>	7.72e-05	9.86e+00	2.66e+01
	$G_6$	<b>1.28e-20</b>	1.11e-09	1.49e-10	4.32e-01
	$G_7$	<b>2.11e-04</b>	2.82e-04	7.22e-03	1.21e-03
	$G_8$	1.19e+03	<b>6.31e+03</b>	1.91e+03	4.19e+03
	$G_9$	<b>0.00e+00</b>	<b>0.00e+00</b>	1.14e+01	2.05e+00
	$G_{10}$	<b>0.00e+00</b>	<b>0.00e+00</b>	3.69e+00	3.47e-03
Standard deviation	$G_1$	<b>0.00e+00</b>	<b>0.00e+00</b>	1.95e-07	1.32e-32
	$G_2$	<b>3.06e-101</b>	7.06e-91	2.91e-18	4.49e-20
	$G_3$	<b>1.32e-125</b>	7.94e-121	7.75e-04	6.43e-08
	$G_4$	<b>3.15e-92</b>	2.67e-86	1.34e-01	3.21e-08
	$G_5$	<b>2.38e-07</b>	1.64e-04	2.05e+01	5.77e-01
	$G_6$	<b>2.41e-20</b>	2.37e-09	5.36e-10	2.72e-01
	$G_7$	<b>1.81e-04</b>	2.31e-04	5.01e-03	4.71e-04
	$G_8$	<b>6.57e-01</b>	3.56e+02	1.91e+02	2.41e+02
	$G_9$	<b>0.00e+00</b>	<b>0.00e+00</b>	3.67e+00	2.75e+00
	$G_{10}$	<b>0.00e+00</b>	<b>0.00e+00</b>	8.89e-01	7.52e-03

**Table 4.** Pair-wise Wilcoxon signed rank test results.

Problem	LTC-SSA/GWO	LTC-SSA/PSO	LTC-SSA/SSA
$G_1$	7.55e-10	7.55e-10	3.43e-03
$G_2$	7.55e-10	7.55e-10	6.12e-03
$G_3$	7.55e-10	7.55e-10	6.12e-03
$G_4$	7.55e-10	7.55e-10	7.55e-10
$G_5$	7.55e-10	7.55e-10	9.07e-10
$G_6$	7.55e-10	2.33e-03	7.55e-10
$G_7$	1.38e-09	7.55e-10	8.37e-03
$G_8$	1.31e-09	7.55e-10	7.55e-10
$G_9$	1.41e-09	7.55e-10	NA
$G_{10}$	2.44e-04	7.55e-10	NA
+ / = / -	<b>10 / 0 / 0</b>	<b>10 / 0 / 0</b>	<b>8 / 2 / 0</b>

mixture (Nezamirad, Yazdi et al. 2022). However, due to discrepancies in the density and pressure gradients during the expansion and compression of vapor bubbles, this model makes it challenging to capture the impact of baroclinic torque. In the present work, the transport equation-based model was adopted.

The Schnerr-Sauer cavitation model, which is adequate for complicated orifice flow circumstances, is used to model the source terms  $\dot{R}_e$  and  $\dot{R}_c$  given above (Guo, He et al. 2017, Yu, Goldsworthy et al.

2017). Condensation and vaporization rates are defined as follows:

$$\begin{cases} \dot{R}_e = \frac{\rho_l \rho_v}{\rho} \alpha_v \alpha_l \frac{3}{R_b} \sqrt{\frac{2}{3} \frac{(P_v - P)}{P_l}} (P_v \geq P) \\ \dot{R}_c = \frac{\rho_l \rho_v}{\rho} \alpha_v \alpha_l \frac{3}{R_b} \sqrt{\frac{2}{3} \frac{(P - P_v)}{P_l}} (P_v \leq P) \end{cases} \quad (17)$$

where the saturation vapor pressure of liquid is defined as  $P_v$ , and  $\rho$  is the density of the mixture defined as  $\rho = \alpha_l \rho_l + \alpha_v \rho_v + \alpha_i \rho_i$ . The definition of  $\alpha_v$  is shown in Eq. (14), which expresses the relationship between the number of bubbles per unit volume  $N_b$  of pure liquid



and the bubble radius  $R_B$ .

$$\alpha_v = \frac{N_b \frac{4}{3} \pi R_B^3}{1 + n \frac{4}{3} \pi R_B^3} \quad (18)$$

$$R_B = \left( \frac{3\alpha_v}{4\pi n (1 - \alpha_v)} \right)^{\frac{1}{3}} \quad (19)$$

Here, the only required input parameter  $N_b$  for the numerical solution was assigned as default value of  $10^{12}$ , and it was testified that this is an optimal value (Liu, Liu et al. 2012). The density of bubble nuclei in the fluid strongly relates to the bubble number density. According to conclusion drawn by Li, Pourquie et al. (2014), it was found the vapor volume appears to be unaffected by the higher bubble density than the default amount. On the other hand, a smaller bubble density is likely to indicate an enormous vapor volume. The overshoot in source intensity fluctuations, proportional to bubble density, might be one plausible explanation for this occurrence. This overshoot appears to be a pseudo-proposition cavitation model with little to do with physics. As a result, in this investigation, the default value of  $N_b = 10^{12}$  is employed.

### 3.3.2. Turbulence model

In order to choose an appropriate turbulence model for the numerical simulations, the result comparison associated with three different turbulence models, i.e., *SST k- $\omega$* , *RNG k- $\epsilon$* , and *Realizable k- $\epsilon$*  models, is shown in Figure 7, where the radial distribution of wall shear stress,  $2\tau_w/\rho v_0$ , is illustrated on the  $y$ -axis. Although the differences among attributed to different turbulence models are observable, their radial distributions have the same trend from experimental observation when  $2 < r/b < 9$ , where  $r$  is the distance from 'O' on the target wall shown in Figure 6, and  $b$  is the half-width of the impingement pressure profile (Loureiro and Freire 2012). By comprehensive comparison with experiments (Poreh, Tsuei et al. 1967, Loureiro and Freire 2017), the predicted values of through simulation cases via *RNG k- $\epsilon$*  model agree well with the experimental results, rather than cases related to the other two turbulence models. In addition, Li, Zheng et al. (2017) and Celik, Ozden et al. (2014) verified that the *RNG k- $\epsilon$*  model can get favourable results in the CFD simulations concerning cavitation flow. Here, the *RNG k- $\epsilon$*  turbulence model was adopted to evaluate the hydrodynamic performance of UHP water jet nozzle.

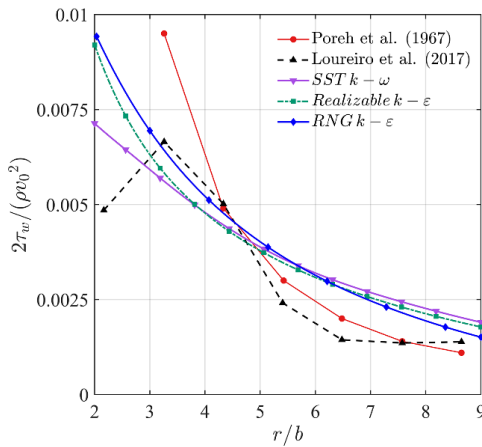


Figure 7. Correlation between computational and experimental values.

Yakhot and Orszag (1986) developed *RNG k- $\epsilon$*  turbulence model, which is capable of simulating flows with high strain rates and huge curvature with acceptable accuracy. The following transport equations are used to calculate the turbulence kinetic energy  $k$  and the

rate of dissipation  $\epsilon$ :

$$\frac{\partial}{\partial t} (\rho k) + \frac{\partial (\rho k u_i)}{\partial x_i} = \frac{\partial}{\partial x_j} \left[ \alpha_k \mu_{eff} \frac{\partial k}{\partial x_j} \right] + G_k - \rho \epsilon \quad (20)$$

$$\frac{\partial}{\partial t} (\rho \epsilon) + \frac{\partial (\rho \epsilon u_i)}{\partial x_i} = \frac{\partial}{\partial x_j} \left[ \alpha_\epsilon \mu_{eff} \frac{\partial \epsilon}{\partial x_j} \right] + C_{1\epsilon} G_k \frac{\epsilon}{k} - C_{2\epsilon} \rho \frac{\epsilon^2}{k} \quad (21)$$

where  $G_k$  is the turbulence kinetic energy generated as mean velocity gradients. The  $C_{1\epsilon}$  and  $C_{2\epsilon}$  coefficients are set to be 1.42 and 1.68 in default respectively. For  $k$  and  $\epsilon$ , the values  $\alpha_k$  and  $\alpha_\epsilon$  are the inverse effective Prandtl numbers. The effective viscosity  $\mu_{eff}$  in the case of a high Reynolds number is stated as:

$$\mu_{eff} = \mu + \mu_t \quad (22)$$

$$\mu_t = \rho C_\mu \frac{k^2}{\epsilon} \quad (23)$$

### 3.4. Grid-independency study

The grid density has a significant impact on the accuracy of numerical simulation. Undoubtedly, a refined mesh can improve the simulation accuracy of the impinging process for the UHP water jet. For high-speed multiphase flow simulations, the grid density should simultaneously cater to the accuracy requirement and speed calculation. Therefore, there are strict requirements for mesh quality inside the volumes where the speed of multiphase media is high, or the phases change rapidly, e.g. contraction field. On the other hand, a coarse mesh can be adopted surrounding the refined mesh volumes. The graded hexahedral grid topology is suitable for this kind of computational domain with significant differences in speed and phase, because it can provide more accurate solution to the flow field interested and spend less time to solve the fluid field unconcerned. According to the knowledge of fluid mechanics, a more satisfactory mesh resolution is used in the domain center neighborhood. As the distance from the centerline increases, the mesh resolution becomes coarser, as shown in Figure 8.

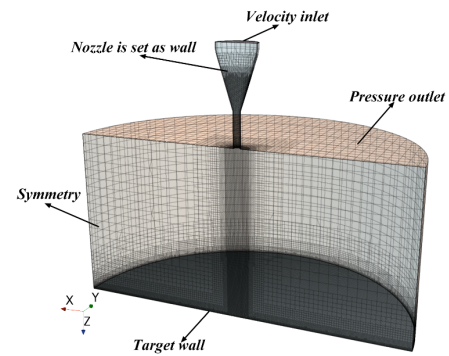


Figure 8. Correlation between computational and experimental values.

Grid-independency analysis was carried out firstly to quantify the effect of the proposed CFD model on the numerical simulation results. Based on the same mesh topology scheme, four simulation cases with increasing grid density, namely Mesh-1 to Mesh-4, were performed. The mesh configurations of the proposed CFD model and the obtained maximum pressure are shown in Table ???. As seen in the Table ???, the maximum pressure value achieved using Mesh-3 is similar to that obtained via Mesh-4, indicating that increasing the number of mesh cells does not affect the calculation results, once a certain number of mesh cells is reached. The total number of elements is estimated to be around 1.3 million, with an average element quality of 0.97. Hence, the mesh topology and grid density utilized in Mesh-3 were employed in the following numerical simulations.

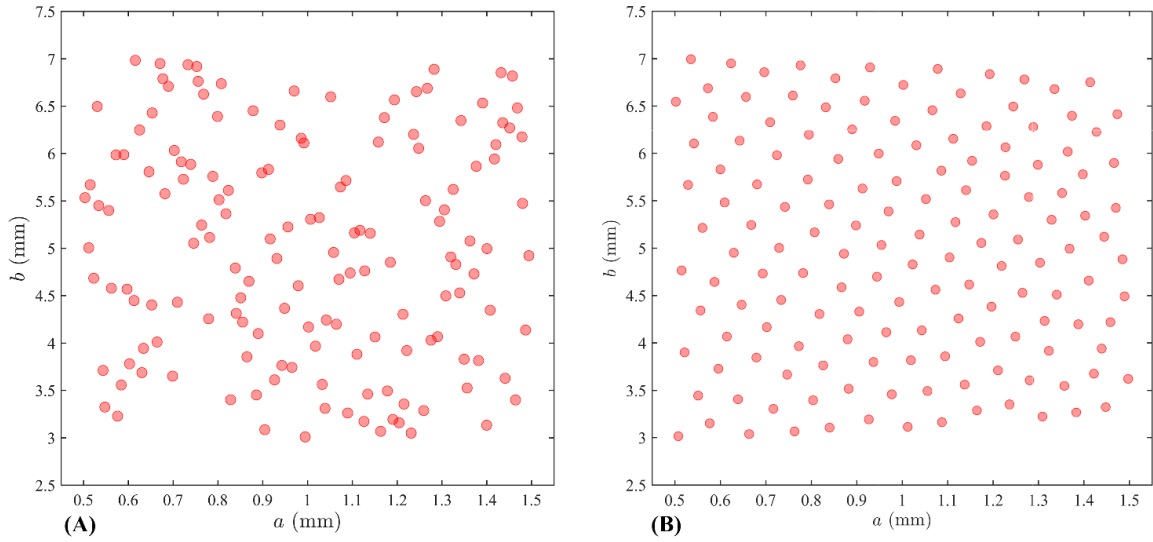


Figure 9. Correlation between computational and experimental values.

## 4. The establishment of approximation method for CFD data

### 4.1. Design of experiment (DOE)

To improve optimization speed, an approximate relation between design variables and responses is often established using the surrogate model method in place of many CFD calculations. This method is widely used in engineering optimization design because of its simplicity and efficiency. Generating a set number of sample points is an important task for constructing the surrogate model and how to generate these sample points is related to the design of experiments (DOE). There are many DOE methods currently available, including orthogonal design, full-factorial design, central composite design, and Latin hypercube design (LHD) (McKay, Beckman et al. 2000), etc. The optimal Latin hypercube design (Opt LHD) is one of the DOE techniques that has been widely utilized to build response surface approximation (Duan, Wang et al. 2017). The Opt LHD method generates an initial design matrix  $X$  denoted by  $m \times n$  LHD, which contains  $m$  test points and  $n$  factors, and then update the design matrix through element exchange.

$$d(x_i, x_j) = d_{ij} = \left[ \sum_{k=1}^n |x_{ik} - x_{jk}|^t \right]^{\frac{1}{t}} \quad (24)$$

where  $p = 1$  or  $2$ ,  $1 \leq i, j \leq m$ ,  $i \neq j$ , the sampling point  $d(x_i, x_j)$  is the minimum distance between  $x_i$  and  $x_j$ .

In this paper, the optimal Latin hypercube design (Opt LHD) (Yang and Cao 2020) is adopted and the results of the comparison between LHD and Opt LHD methods is illustrated in Fig. 9. It can be found that the Opt LHD method makes all sample points to be more evenly distributed in the design space, compared to the LHD method. Thus, the Opt LHD method features superior space-filling and evenness, and allows for more accurate surrogate models between design variables and responses.

Based on the Opt LHD method, 150 schemes are designed to calculate the peak wall shear stress, as shown in Appendix 1. The space distributions of samples are shown in Figure 10. The peak wall shear stress is calculated by CFD method in Section 3.

### 4.2. Data-driven surrogate model

In the process of optimizing the nozzle structure, the optimizer solves the CFD model several times to evaluate the objective function. In terms of computational time, CFD-based design methods are very expensive owing to requirement for numerous simulations. Thus,

the SVM-based method is used to develop a data-driven surrogate model in this section.

#### 4.2.1. Support Vector Machine (SVM)

The SVM is a new AI algorithm proposed by Cortes and Vapnik (1995) and it has distinct advantages in handling nonlinear regression and small samples. As shown in Figure 10, The core concept of SVM is to find a separating Hyperplane used to divide the space into two sides via maximizing the margin or the distance from the hyperplane to the closest samples (Tran, Tempel et al. 2015). A nonlinear mapping function  $\phi(x)$  are used to map low-dimensional  $i$ -th input sample  $x_i$  into higher-dimensional vector spaces for a given dataset. Based on the linear regression function established in high-dimensional space, the following equation can be derived:

$$f(x) = \omega \cdot \phi(x) + bx, x \in R^d, b \in R \quad (25)$$

where  $d, R, \omega, b, x$  and  $\phi(x)$  are the dimensionality of the sample space, the set of real numbers, weight coefficients, bias values, input vector in the sample space and predictive values, respectively. Based on the theory of structural risk minimization principle, the problem of support vector regression (SVR) is cast into a constrained optimization problem, shown in Eqs. (26) and (27) (Chang and Lin 2011), which is also known as primal problem.

$$\min_{\omega, b, \xi} \frac{1}{2} \|\omega\|^2 + C \sum_{i=1}^n (\xi_i + \xi_i^*) \quad (26)$$

$$\text{s.t. } -\varepsilon - \xi_i \leq y_i - (\omega^\top x_i + b) \leq \varepsilon + \xi_i^* \quad (27)$$

$$\xi_i, \xi_i^* \geq 0, i = 1, 2, \dots, n$$

where  $n, \xi_i, \xi_i^*$ , and  $C$  are the number of samples, slack variable of upper bound, slack variable of lower bound, the constant deviation and the penalty coefficient, respectively.

#### 4.2.2. The proposed LTC-SSA-SVM model

The detailed steps of the proposed LTC-SSA-SVM model are provided below.

*Step1:* First, the dataset is prepared for the creation and validation of the SVM model. Then, the dataset was randomly partitioned into a training (70%) and test dataset (30%). These percentages are selected primarily because they provide the lowest error for the SVM model.

*Step2:* Initialize the parameters related to the SSA algorithm, including the number of sparrows  $n_s$ , producer ratios  $P_D$ , number of iterations  $M$ , the alarm value  $R_2$ , and safety threshold  $S_T$ .

*Step3:* Define the objective function. The fitness function  $G$  is

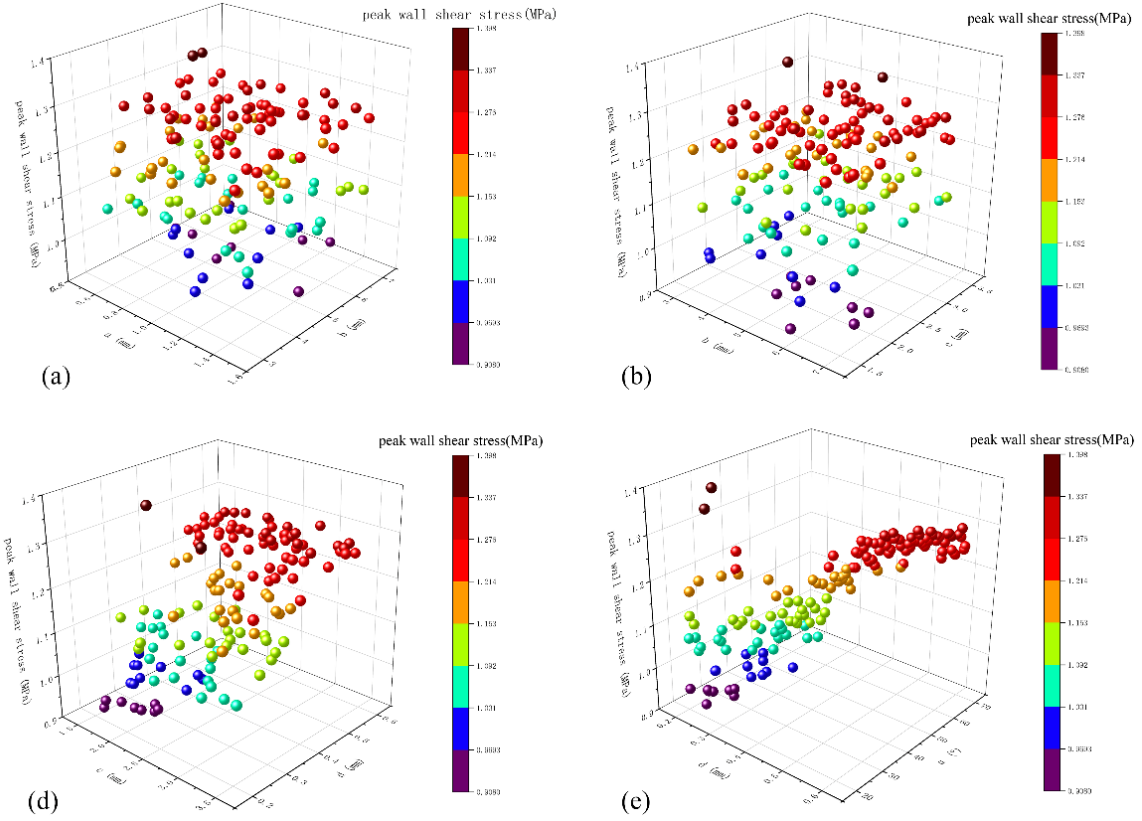


Figure 10. Correlation between computational and experimental values.

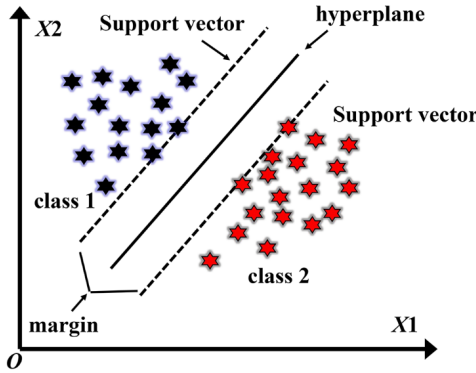


Figure 11. Concept of the SVM algorithm.

taken as the mean square error (MSE) of training sets given by Eq. (28). If the stopping criterion is satisfied, the position of the sparrow with the lowest fitness is the optimal solution of the model.

$$MSE = \frac{1}{n} \sum_{i=1}^n (P_i - O_i)^2 \quad (28)$$

where  $P_i$  is the predicted value of  $i$ -th peak wall shear stress by SVM,  $O_i$  is the expected value of  $i$ -th peak wall shear stress by CFD method.

*Step4:* Initialize the position of sparrows randomly using the improved LTC map. *Step5:* Update the location of producers and scroungers. *Step6:* Select the guards and renew their locations. *Step7:* Calculate the fitness levels of the updated sparrows. *Step8:* Update the current optimal solution according to the fitness of the sparrows. *Step9:* Determine whether the iteration of algorithm is ended. If not, return to Step 5. *Step10:* To achieve the goal of effectively forecasting the results of peak wall shear stress, the optimal result is used to train the hyper-parameter  $C$  and  $g$  for SVM model.

### 4.3. Validation of the LTC-SSA-SVM model

To evaluate the feasibility of the proposed model in section 4.2, two data-driven surrogate models, namely SVM and LTC-SSA-SVM, have been developed in MATLAB using the samples from Appendix 1. Subsequently, both of these models are used to predict the peak wall shear stress. A comparison between the calculated and the predicted values of peak wall shear stress related to SVM and LTC-SSA-SVM models are shown in subplots (a-d) of Figure 12. Obviously, it can be found that the predicted results of LTC-SSA-SVM model on the training and testing sets show better agreement with the calculated values, compared to those of SVM model.

To further quantify the performance of the proposed LTC-SSA-SVM model, the statistics performance comparison among the SVM, LTC-SSA-SVM, BPNN (Chen and Chen 2022), GBDT (Swami and Jain 2013) and RBFNN (Cai, Hocine et al. 2021) is made using different statistical measures. The  $RMSE$ ,  $MAE$ ,  $NSE$  and  $R^2$  are some of these indicators, and the formulas used for these indicators calculations are provided below (Cai, Hocine et al. 2021).

$$MSE = \frac{1}{n} \sum_{i=1}^n (P_i - O_i)^2 \quad (29)$$

$$MAE = \frac{1}{n_e} \sum_{i=1}^{n_e} |O_i - P_i| \quad (30)$$

$$NSE = 1 - \frac{\sum_{i=1}^{n_e} (O_i - P_i)^2}{\sum_{i=1}^{n_e} (O_i - \bar{O}_i)^2} \quad (31)$$

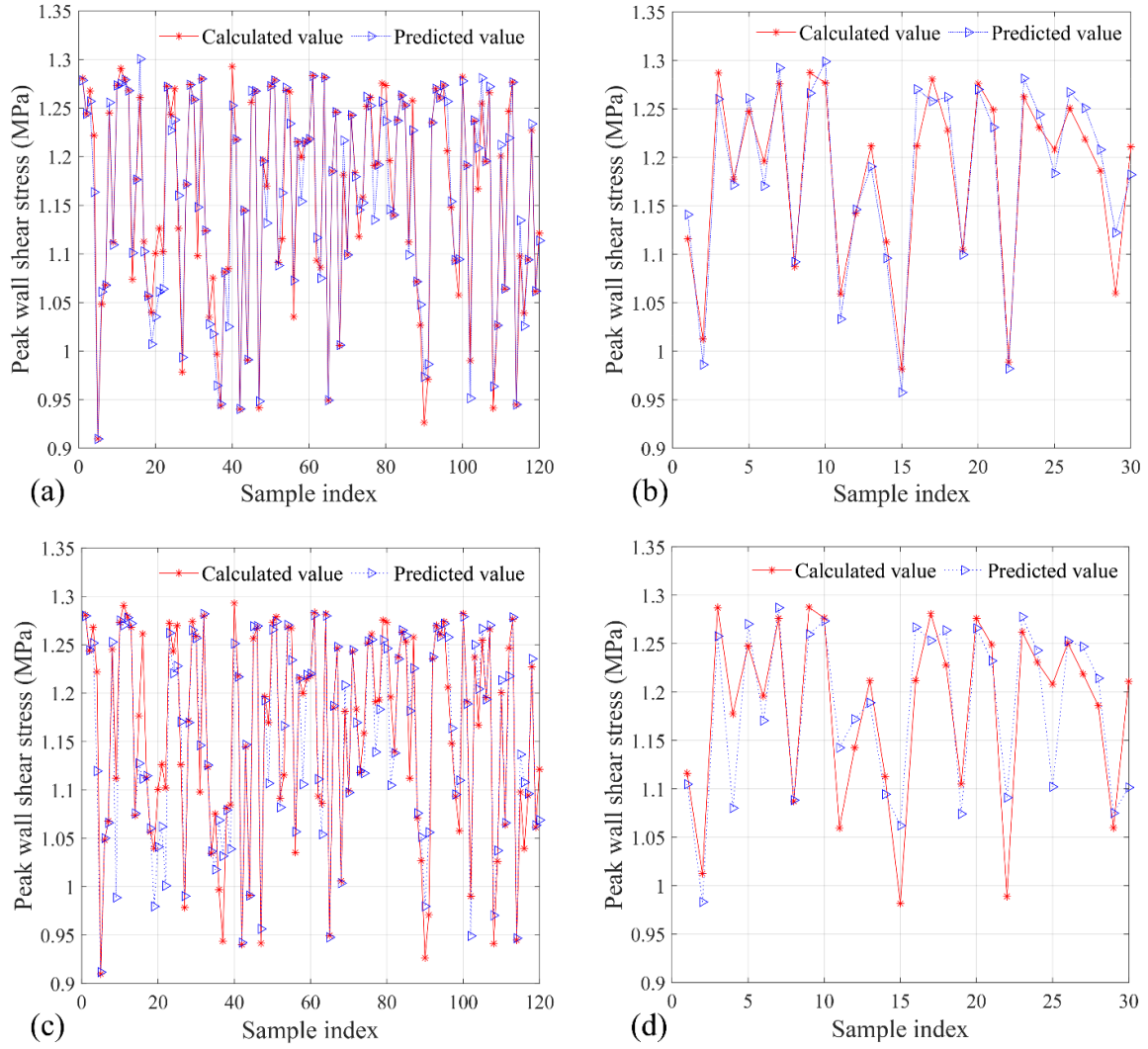


**Figure 12.** Prediction results of peak wall shear stress (a) LTC-SSA-SVM training sets, (b) LTC-SSA-SVM testing sets, (c) SVM training sets and (d) SVM testing sets.

$$R^2 = 1 - \frac{\left( \sum_{i=1}^{n_e} (O_i - \bar{O}_i) (P_i - \bar{P}_i) \right)^2}{\sum_{i=1}^{n_e} (O_i - \bar{O}_i)^2 \sum_{i=1}^{n_e} (P_i - \bar{P}_i)^2} \quad (32)$$

where  $n_e$  is the number of samples,  $\bar{P}_i$  and  $\bar{O}_i$  represent the predicted and calculated mean values of the peak wall shear stress, respectively. Notably, the prediction model with the lowest *RMSE* and *MAE* values corresponds to a greater accuracy. However, it with the greatest *NSE* and  $R^2$  values corresponds to a more robust and efficient performance.

Algorithm	RMSE	$R^2$	NSE	MAE
LTC-SSA-SVM	0.024	0.95	0.95	0.014
SVM	0.041	0.85	0.85	0.023
BPNN	0.045	0.82	0.81	0.028
GBDT	0.047	0.74	0.74	0.032
RBFNN	0.063	0.71	0.63	0.019

**Table 5.** Statistics performance comparison based on the different models.

Table 5 summarizes the calculated *RMSE*, *NSE*, *MAE* and  $R^2$  results of the statistical indicators. As shown in Table 5, it can be found that the proposed LTC-SSA-SVM model with *MSE* of 0.024,  $R^2$  of 0.95 *NSE* of 0.95 and *MAE* of 0.014, is superior to the other

four models. All the statistical results adequately demonstrate the accuracy and reliability of LTC-SSA-SVM model.

A comparison of regression coefficient  $R^2$  between the SVM and LTC-SSA-SVM models are shown in subplots (a) and (b) of Figure 13. The  $R^2$  (value ranges from 0 to 1) is used to measure the goodness of fit related to model, and the  $R^2$  value nearer to value one indicates a better prediction effect. The blue and orange solid line represents the linear regression of training and test sets respectively, whereas the black dashed line shows a near-perfect forecast. As shown in Figure 11, it can be found that LTC-SSA-SVM model exhibits larger  $R^2$  values (i.e., 0.952 and 0.9318) in the training and testing phases, compared to SVM model. Training results are satisfactory for LTC-SSA-SVM model, and the  $R^2$  values are greater than 0.9 for training and testing, phases.

## 5. Nozzle structure optimization problems

For different chamber structure of UHP nozzle obtained by varying geometry parameters (i.e.,  $a, b, c, d, \theta$ ), it is likely that the recognized best hydrodynamic performance could be biased. Thus, it is necessary to develop a strategy to find an optimal combination of geometric parameters for obtaining optimal hydrodynamic performance.

### 5.1. Optimize processes

In this study, an optimization scheme for improving the chamber structure of the UHP nozzle is proposed, as shown in Figure 14. The

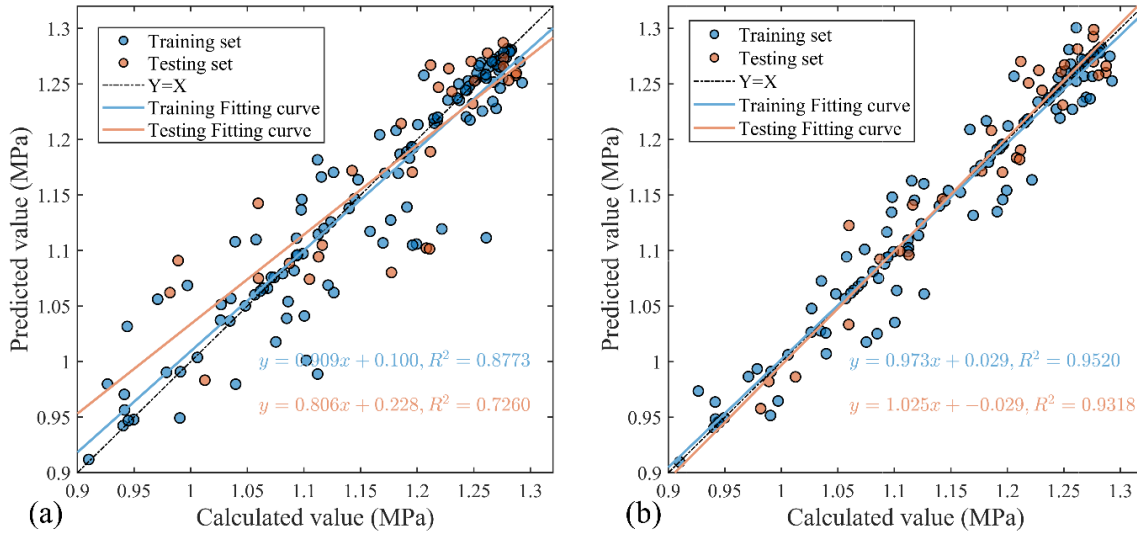


Figure 13. Regression coefficient plot of SVM (a) and LTC-SSA-SVM (b) models.

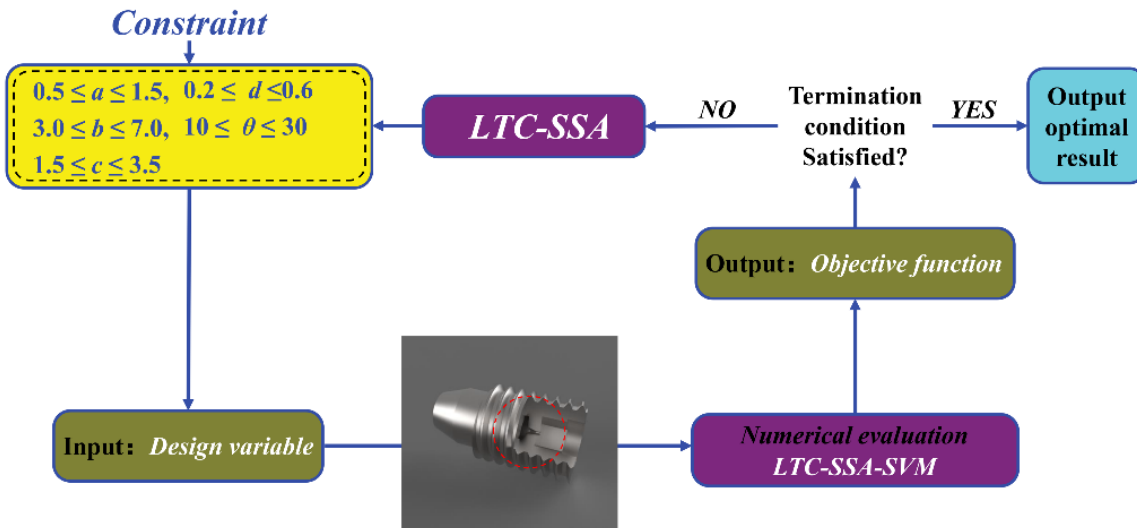


Figure 14. Flow chart of the optimization loop.

detailed steps are as follows:

*Step1:* Update a set of design variables (i.e.,  $a, b, c, d, \theta$ ) using the LTC-SSA algorithm under constraint conditions.

*Step2:* Calculate the values of peak wall shear stress (i.e., the fitness of each sparrow) corresponding to this set of design variables using LTC-SSA-SVM model.

*Step3:* Update the global optimal solution according to the fitness of the sparrows.

*Step4:* Steps 1-3 are repeated until the LTC-SSA algorithm reached a pre-defined stopping criterion.

### 5.2. Optimization strategy

The objective function is the peak wall shear stress calculated via an approximation model mentioned in Section 4. The design variables (i.e.,  $a, b, c, d, \theta$ ) have been shown in Table 6. Details about parameters of LTC-SSA algorithm are to be presented in section 2.4.1. In addition, the population size is set to 30 and The maximum number of iterations is set to 80. The optimization procedure is conducted on Intel Core i5-4210U CPU @1.70GHz, 16GB RAM.

### 5.3. Results and discussion

The convergence history of peak wall shear stress obtained using the LTC-SSA algorithm is presented in Figure 15. The optimized

No.	Design variables	Lower value	Upper value
1	$a$	0.5	1.5
2	$b$	3.0	7.0
3	$c$	1.5	3.5
4	$d$	0.2	0.6
5	$\theta$	10	35

Table 6. Ranges of design variables.

model showed an increase of 9.41% in peak wall shear stress. This result indicates that finding the optimal combination of geometric parameters significantly enhances the hydrodynamic performance of the UHP nozzle. Therefore, the LTC-SSA algorithm proposed in this study is a promising method for UHP nozzle optimization.

Table 7 presents the optimal solution of a nozzle structure optimization problem obtained via using the proposed LTC-SSA algorithm. As shown in Table 7, It can be found that the access section length ( $a$ ), exit section length ( $c$ ), outlet radius ( $d$ ) and contraction angle ( $\theta$ ) increase, whereas the contraction section length ( $b$ ) decrease. Figure 16 shows a comparison of the geometry for the original model and the optimal model.

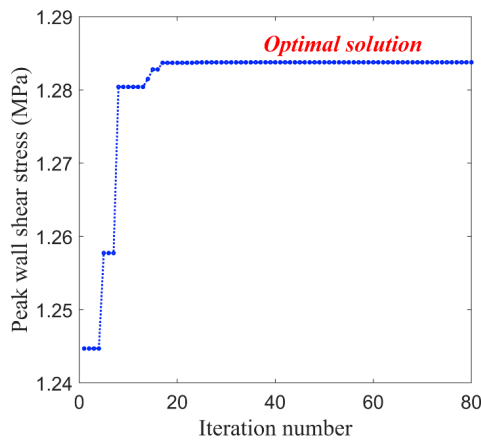


Figure 15. Convergence history of the peak wall shear stress by LTC-SSA algorithm.

Original	Optimal	Increase or decrease	
a (mm)	1.0	1.044	Increase
b (mm)	5.0	3.326	Decrease
c (mm)	2.5	2.694	Increase
d (mm)	0.4	0.504	Increase
$\theta$ (°)	22.5	30.605	Increase

Table 7. The optimal solution as well as the original geometry parameters.

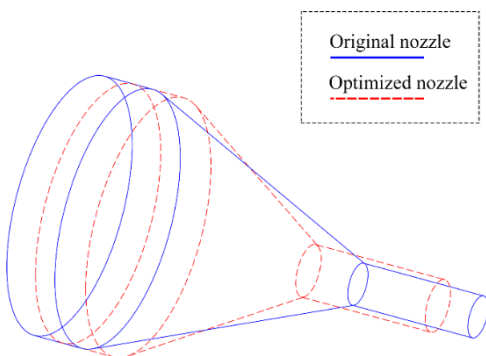


Figure 16. A comparison of the geometry structure between original and optimized nozzles.

The comparison of the velocity distribution contours between original and optimal models is illustrated in Figure 17. As shown in Figure 17, it can be observed that, due to the Bernoulli effect, both of them form a core high-speed region at the exit section and the maximum flow velocity is not significantly different. The radial flow velocity is maximum in the water-jet central axis, and gradually decreases toward the periphery regions. The diffusion zone interacts with the surrounding low-velocity fluid to form the turbulent boundary layer, where energy is dissipated and the velocity is reduced. The core velocity region of the original nozzle is relatively concentrated, narrow and longer, so the free space in the diffusion section is large. However, the core velocity region of the optimized nozzle has a larger coverage area in the diffusion section, resulting in a relatively faster diffusion.

Figure 18 shows the comparison of the axial distribution of velocity between original and optimal models. It can be found that the axial maximum velocity is equal to the maximum velocity of the entire flow field, indicating that the position where the flow velocity is largest

appears on the axis, and a significant difference in the trends can be observed. For the axial velocity distribution of the original model, the velocity reaches a peak in the cylindrical section and forms the core constant velocity zone. Then the velocity drops slightly outside the nozzle outlet. Subsequently, there is a significant decrease as the axial distance increases. However, the axial velocity distribution of the optimized model is very different. There is a distinct two-order constant velocity section. In the cylindrical section, the increase of speed is significantly lower than before, and the maximum speed of the axis is reached at the exit of the cylindrical section. The first segment of the constant velocity region is then formed within the diffusion segment. The first significant velocity drop occurs at the exit of the diffuser section, followed by the second constant velocity zone. The total length of the two constant velocity segments is similar to that of the original model. Subsequently, as the x-axial distance increases, a significant speed reduction occurs. The impact kinetic energy of the optimized nozzle is reduced faster, but the fatigue action of the micro jet for med by the bubble collapse is the main destructive factor.

Figure 19 shows the comparison of radial wall-shear-stress distribution between original and optimized nozzles. As clearly seen from Figure 19, the optimal model shows a good cavitation performance and the radial peak wall shear stress is increased by 0.829%, compare with original nozzle.

## 6. Conclusion

This paper proposes a CFD-based design procedure to optimize the geometry structure of UHP water-jet nozzles. The RANS solver is used to analyze wall shear stress and impinging force, with validation through experimental data. The proposed optimization method integrates the LTC map, Opt LHD method, SVM-based surrogate model, and SSA algorithm. In addition, the main innovations and contributions of this paper are summarized as follows:

1)The standard SSA algorithm faces the challenge of getting stuck in local optima. To address this issue, authors have embedded the LTC map, which combines the benefits of Logistic and Tent chaotic maps, into the SSA algorithm. This modification aims to enhance the diversity of the initial population. The effectiveness of the proposed LTC-SSA algorithm was verified by 10 constraint benchmark functions, and compared with SSA, GWO and PSO algorithms. The results demonstrate that the LTC-SSA algorithm can significantly improve the reliability of global optimality and the quality of the results.

2)To save calculation costs during sample set construction, only half of the computational model was used instead of the complete model. The results showed good agreement between the simulation results and the measured wall impinging forces, with numerical errors below 1.1%.

3)To expedite optimization speed, a design of experiments (DOE) is used to establish an approximate relationship between design variables and responses. This is done by replacing numerous CFD calculations with a LTC-SSA-SVM-based surrogate model. The results indicate that the Opt LHD method has better space-filling and evenness than the LHD method. Furthermore, the data-driven surrogate model demonstrates that the proposed LTC-SSA-SVM model outperforms the SVM, BPNN, GBDT, and RBFNN models, with a  $MSE$  of 0.024,  $R^2$  of 0.95,  $NSE$  of 0.95, and  $MAE$  of 0.014.

This paper describes the optimization of the geometry structure of a UHP water-jet nozzle using the LTC-SSA algorithm. The optimized structure resulted in a high-wall-shear-stress nozzle with superior hydrodynamic performance, increasing the peak wall shear stress of the optimal solution by 9.41% compared to the original design. While the proposed optimized-protocols for UHP water-jet nozzle show great promise and feasibility in engineering applications, it is important to note that this study only investigated one specific type of nozzle with a relatively simple geometric structure, limiting its generalizability. The main objective in the near future is to expand

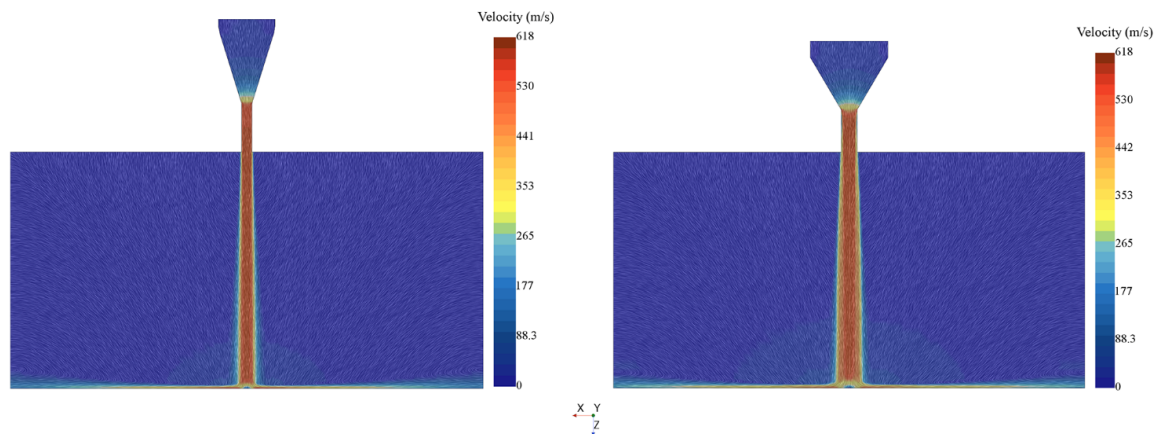


**Figure 17.** A comparison of velocity distribution contours between original and optimized nozzles.

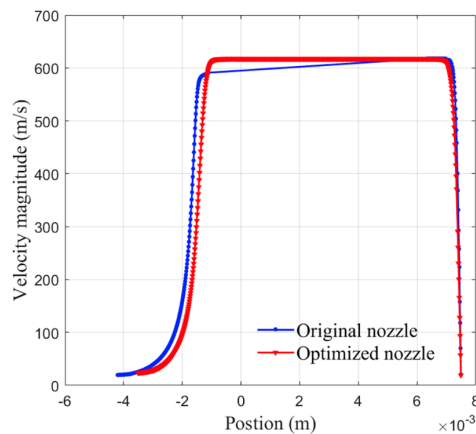


**Figure 18.** A comparison of axial velocity distribution between original and optimized nozzles.

this framework to include more types of nozzles. This can greatly inspire the design of more efficient nozzles.

## References

- [1] Arora, S., & Singh, S. (2019). Butterfly optimization algorithm: a novel approach for global optimization. *Soft Computing*, 23, 715-734.
- [2] Cai, M., Hocine, O., Mohammed, A. S., Chen, X., & Hasani-panah, M. (2021). Integrating the LSSVM and RBFNN models with three optimization algorithms to predict the soil liquefaction potential. *Engineering with Computers*, 3, 1-13.
- [3] Celik, F., Ozden, Y. A., & Bal, S. (2014). Numerical simulation of flow around two- and three-dimensional partially cavitating hydrofoils. *Ocean Engineering*, 78, 22-34. <https://doi.org/10.1016/j.oceaneng.2013.12.016>
- [4] Chang, C.-C., & Lin, C.-J. (2011). LIBSVM: a library for support vector machines. *ACM Transactions on Intelligent Systems and Technology (TIST)*, 2(3), 1-27.
- [5] Chen, Y.-J., & Chen, Z.-S. (2022). A prediction model of wall shear stress for ultra-high-pressure water-jet nozzle based on hybrid BP neural network. *Engineering Applications of Computational Fluid Mechanics*, 16(1), 1902-1920. <https://doi.org/10.1080/19942060.2022.2123404>
- [6] Cortes, C., & Vapnik, V. (1995). Support-Vector Networks. *Machine Learning*, 20(3), 273-297.
- [7] Dhiman, A., & Toshniwal, D. (2020). An approximate model for event detection from twitter data. *IEEE Access*, 8, 122168-122184.
- [8] Duan, B., Wang, Q., Zeng, X., Gong, Y., Song, D., & Wang, J. (2017). Calibration methodology for energy management system of a plug-in hybrid electric vehicle. *Energy Conversion and Management*, 136, 240-248.
- [9] Feldman, A., Provan, G., & Van Gemund, A. (2010). Approximate model-based diagnosis using greedy stochastic search. *Journal of Artificial Intelligence Research*, 38, 371-413.
- [10] Ghalandari, M., Ziamolki, A., Mosavi, A., Shamshirband, S., Chau, K.-W., & Bornassi, S. (2019). Aeromechanical optimization of first row compressor test stand blades using a hybrid machine learning model of genetic algorithm, artificial neural networks and design of experiments. *Engineering Applications of Computational Fluid Mechanics*, 13(1), 892-904.
- [11] Gu, Q., Chang, Y., Li, X., Chang, Z., & Feng, Z. (2021). A novel F-SVM based on FOA for improving SVM performance. *Expert Systems with Applications*, 165, 113713.
- [12] Gu, Y., Yu, S., Mou, J., Wu, D., & Zheng, S. (2020). Research Progress on the Collaborative Drag Reduction Effect of Polymers and Surfactants. *Materials (Basel)*, 13(2), 444. <https://doi.org/10.3390/ma13020444>
- [13] Gu, Y. Q., Mou, J. G., Dai, D. S., Zheng, S. H., Jiang, L. F., Wu, D. H., Ren, Y., & Liu, F. Q. (2015). Characteristics on drag reduction of bionic jet surface based on earthworm's back orifice jet. *Acta Physica Sinica*, 64(2), 024701. <https://doi.org/10.7498/aps.64.024701>
- [14] Guo, G. M., He, Z. X., Chen, Y. H., Wang, Q., Leng, X. Y., & Sun, S. X. (2017). LES investigations on effects of the residual bubble on the single hole diesel injector jet. *International Journal of Heat and Mass Transfer*, 112, 18-27. <https://doi.org/10.1016/j.ijheatmasstransfer.2017.04.080>
- [15] Harimoorthy, K., & Thangavelu, M. (2021). Multi-disease prediction model using improved SVM-radial bias technique in healthcare monitoring system. *Journal of Ambient Intelligence and Humanized Computing*, 12, 3715-3723.
- [16] Herulambang, W., Hamidah, M. N., & Setyatama, F. (2020). Comparison of svm and bpnn methods in the classification of batik patterns based on color histograms and invariant moments. In *2020 International Conference on Smart Technology and Applications (ICoSTA)*.

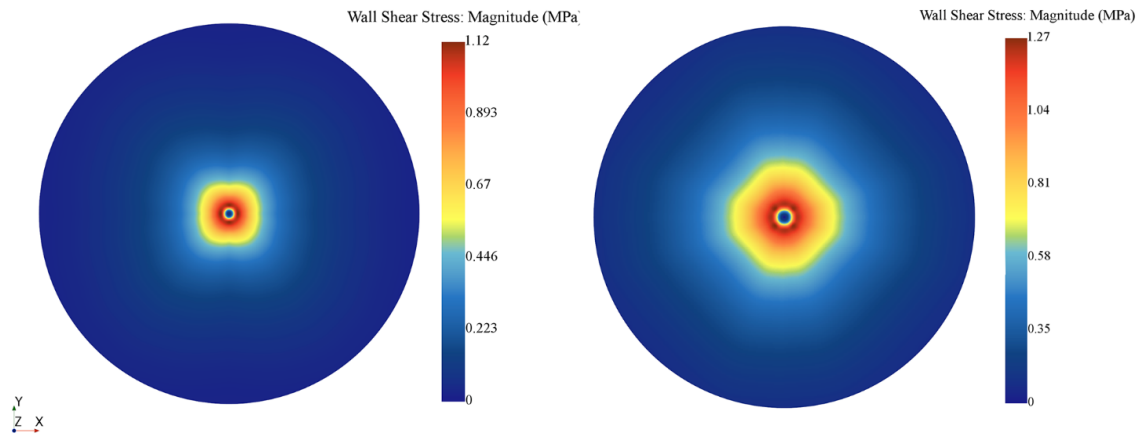


**Figure 19.** A comparison of radial wall-shear-stress distribution contours between original and optimized.

- [17] Huang, L.-Y., & Chen, Z. S. (2022). Effect of technological parameters on hydrodynamic performance of ultra-high-pressure water-jet nozzle. *Applied Ocean Research*, 129, 103410.
- [18] Jianhua, L., & Zhiheng, W. (2021). A hybrid sparrow search algorithm based on constructing similarity. *IEEE Access*, 9, 117581-117595.
- [19] Jin, Y., Olhofer, M., & Sendhoff, B. (2001). Managing approximate models in evolutionary aerodynamic design optimization. In *Proceedings of the 2001 Congress on Evolutionary Computation (IEEE Cat. No. 01TH8546)*.
- [20] Li, Z., Zheng, D. W., Hong, F., & Ni, D. (2017). Numerical simulation of the sheet/cloud cavitation around a two-dimensional hydrofoil using a modified URANS approach. *Journal of Mechanical Science and Technology*, 31(1), 215-224. <https://doi.org/10.1007/s12206-016-1224-0>
- [21] Li, Z. R., Pourquie, M., & van Terwisga, T. (2014). Assessment of Cavitation Erosion With a URANS Method. *Journal of Fluids Engineering-Transactions of the ASME*, 136(4). <https://doi.org/10.1115/1.4026195>
- [22] Liu, H. L., Liu, D. X., Wang, Y., Wu, X. F., & Zhuang, S. G. (2012). Applicative evaluation of three cavitating models on cavitating flow calculation in centrifugal pump. *Transactions of the Chinese Society of Agricultural Engineering*, 28(16), 54-59.
- [23] Liu, P., Fan, L., Bai, Y., Ma, X., & Song, E. (2015). Modeling and analysis of electromagnetic force approximate model of high-speed solenoid valve. *Transactions of the Chinese Society of Agricultural Engineering*, 31(16), 96-101.
- [24] Liu, W., Sun, K., & Zhu, C. (2016). A fast image encryption algorithm based on chaotic map. *Optics and Lasers in Engineering*, 84, 26-36.
- [25] Loureiro, J., & Freire, A. S. (2012). Wall shear stress measurements and parametric analysis of impinging wall jets. *International Journal of Heat and Mass Transfer*, 55(23-24), 6400-6409.
- [26] Loureiro, J. B. R., & Freire, A. P. S. (2017). Velocity and temperature profiles, wall shear stress and heat transfer coefficient of turbulent impinging jets. *International Journal of Heat and Mass Transfer*, 107, 846-861. <https://doi.org/10.1016/j.ijheatmasstransfer.2016.10.105>
- [27] McKay, M. D., Beckman, R. J., & Conover, W. J. (2000). A comparison of three methods for selecting values of input variables in the analysis of output from a computer code. *Technometrics*, 42(1), 55-61.
- [28] Nezamirad, M., Yazdi, A., Amirahmadian, S., Sabetpour, N., & Hamed, A. (2022). Utilization of Schnerr-Sauer Cavitation Model for Simulation of Cavitation Inception and Super Cavitation. *International Journal of Aerospace and Mechanical Engineering*, 16(3), 36-40.
- [29] Ouyang, C., Qiu, Y., & Zhu, D. (2021). Adaptive spiral flying sparrow search algorithm. *Scientific Programming*, 2021, 1-16.
- [30] Platt, J. C. (1999). Fast Training of Support Vector Machines Using Sequential Minimal Optimization. In *Fast Training of Support Vector Machines Using Sequential Minimal Optimization*.
- [31] Poreh, M., Tsuei, Y. G., & Cermak, J. E. (1967). Investigation of a Turbulent Radial Wall Jet. *Journal of Applied Mechanics*, 34(2), 457-463. <https://doi.org/10.1115/1.3607705>
- [32] Schultz, M. P. (2007). Effects of coating roughness and biofouling on ship resistance and powering. *Biofouling*, 23(5), 331-341.
- [33] Smits, G. F., & Jordaan, E. M. (2002). Improved SVM regression using mixtures of kernels. In *Proceedings of the 2002 International Joint Conference on Neural Networks. IJCNN'02 (Cat. No. 02CH37290)*.
- [34] Sun, S., Cao, Z., Zhu, H., & Zhao, J. (2019). A survey of optimization methods from a machine learning perspective. *IEEE Transactions on Cybernetics*, 50(8), 3668-3681.
- [35] Swami, A., & Jain, R. (2013). Scikit-learn: Machine Learning in Python. *Journal of Machine Learning Research*, 12(10), 2825-2830.
- [36] Tran, V. D. T., Tempel, S., Zerath, B., Zehraoui, F., & Tahi, F. (2015). miRBoost: Boosting support vector machines for microRNA precursor classification. *RNA - a Publication of the RNA Society*, 21(5), 775-785.
- [37] Wang, D., Sun, J., Dong, A., Zhu, G., Liu, S., Huang, H., & Shu, D. (2019). Prediction of core deflection in wax injection for investment casting by using SVM and BPNN. *The International Journal of Advanced Manufacturing Technology*, 101, 2165-2173.
- [38] Wang, W., Wu, Z., Wang, D., & Zhang, W. (2019). A novel surrogate-based aerodynamic optimization method using field approximate model. *Proceedings of the Institution of Mechanical Engineers, Part G: Journal of Aerospace Engineering*, 233(3), 883-895.



- [39] Weichert, D., Link, P., Stoll, A., Rüping, S., Ihlenfeldt, S., & Wrobel, S. (2019). A review of machine learning for the optimization of production processes. *The International Journal of Advanced Manufacturing Technology*, 104(5-8), 1889-1902.
- [40] Wu, C.-C., Weisbrich, S., & Neitzel, F. (2017). Approximate model for geometrical complex structures. *Materials Today: Proceedings*, 4(5), 5995-6000.
- [41] Wu, C.-H., Tzeng, G.-H., Goo, Y.-J., & Fang, W.-C. (2007). A real-valued genetic algorithm to optimize the parameters of support vector machine for predicting bankruptcy. *Expert Systems with Applications*, 32(2), 397-408.
- [42] Xue, J., & Shen, B. (2020). A novel swarm intelligence optimization approach: sparrow search algorithm. *Systems Science & Control Engineering*, 8(1), 22-34.
- [43] Yakhot, V., & Orszag, S. A. (1986). Renormalization group analysis of turbulence. I. Basic theory. *Journal of Scientific Computing*, 1(1), 3-51.
- [44] Yang, L., Li, Z., Wang, D., Miao, H., & Wang, Z. (2021). Software defects prediction based on hybrid particle swarm optimization and sparrow search algorithm. *IEEE Access*, 9, 60865-60879.
- [45] Yang, M., & Cao, B.-Y. (2020). Multi-objective optimization of a hybrid microchannel heat sink combining manifold concept with secondary channels. *Applied Thermal Engineering*, 181, 115592.
- [46] Yu, H., Goldsworthy, L., Brandner, P. A., & Garaniya, V. (2017). Development of a compressible multiphase cavitation approach for diesel spray modelling. *Applied Mathematical Modelling*, 45, 705-727. <https://doi.org/10.1016/j.apm.2017.01.035>
- [47] Zhang, Y., Dou, Z., Veilleux, J. C., Shi, G. H., Collins, D. S., Vlachos, P. P., Dabiri, S., & Ardekani, A. M. (2021). Modeling cavitation bubble dynamics in an autoinjector and its implications on drug molecules. *Int J Pharm*, 608, 121062. <https://doi.org/10.1016/j.ijpharm.2021.121062>
- [48] Zhou, Y., Hua, Z., Pun, C.-M., & Chen, C. P. (2014). Cascade chaotic system with applications. *IEEE Transactions on Cybernetics*, 45(9), 2001-2012.

## 7. Appendix 1

**Table 8.** Experiment samples calculated by CFD

No.	$a(mm)$	$b(mm)$	$c(mm)$	$d(mm)$	$\theta(^{\circ})$	$\tau$ (MPa)	Index	$a(mm)$	$b(mm)$	$c(mm)$	$d(mm)$	$\theta(^{\circ})$	$\tau$ (MPa)
1	0.879	6.050	2.831	0.532	61.478	1.281	76	0.956	6.740	3.468	0.404	45.562	1.218
2	1.284	6.502	1.548	0.489	56.152	1.244	77	1.209	6.922	2.764	0.482	55.279	1.283
3	0.781	4.236	2.067	0.477	54.675	1.268	78	0.514	4.320	2.916	0.360	39.986	1.093
4	0.949	6.655	3.441	0.274	29.294	1.222	79	1.490	5.289	2.572	0.252	26.482	1.086
5	0.825	5.757	1.505	0.225	23.122	0.910	80	0.574	4.374	3.402	0.574	66.776	1.282
6	0.644	4.705	3.071	0.327	34.618	1.116	81	0.689	5.105	1.675	0.203	20.337	0.950
7	1.105	6.296	3.008	0.221	22.595	1.048	82	1.006	3.189	3.288	0.419	47.367	1.185
8	1.151	6.961	1.688	0.344	37.989	1.068	83	1.220	4.026	2.454	0.597	69.617	1.246
9	1.358	4.486	2.790	0.579	67.409	1.245	84	0.867	4.460	2.219	0.245	25.637	1.397
10	1.231	4.993	1.587	0.273	27.914	1.112	85	0.792	6.163	3.198	0.396	44.549	1.181
11	0.839	5.624	1.613	0.315	33.071	1.013	86	0.669	3.374	1.529	0.350	38.716	1.099
12	1.077	4.639	3.059	0.494	56.797	1.287	87	1.352	4.502	1.941	0.566	65.766	1.243
13	0.659	5.657	2.988	0.235	24.323	1.354	88	0.775	6.793	2.412	0.389	43.612	1.183
14	0.512	5.599	3.482	0.542	62.697	1.273	89	0.850	3.850	3.268	0.485	55.601	1.281
15	0.930	6.251	3.378	0.514	59.209	1.248	90	0.535	6.033	2.847	0.339	37.354	1.118
16	1.330	5.499	2.889	0.530	61.195	1.291	91	0.705	4.205	3.207	0.330	36.246	1.158
17	0.680	3.974	3.425	0.552	64.025	1.279	92	1.012	4.900	2.306	0.565	65.653	1.228
18	0.812	4.878	1.746	0.545	63.181	1.268	93	0.734	5.815	1.669	0.492	56.450	1.252
19	1.416	4.749	2.690	0.210	20.011	1.074	94	1.072	5.862	1.559	0.538	62.204	1.261
20	1.436	4.426	2.286	0.413	46.601	1.196	95	1.265	4.768	2.501	0.382	42.765	1.191
21	1.299	6.696	2.528	0.521	60.072	1.276	96	0.890	3.102	2.481	0.418	47.310	1.193
22	1.318	4.356	3.353	0.208	21.054	1.177	97	1.236	4.680	3.037	0.496	57.023	1.275
23	0.842	5.216	3.257	0.275	29.409	1.261	98	1.171	6.386	3.101	0.450	51.248	1.273
24	1.303	3.604	1.973	0.370	41.205	1.113	99	1.497	6.731	2.872	0.281	30.109	1.105
25	0.761	5.038	1.631	0.371	41.351	1.087	100	0.525	5.458	2.977	0.319	34.916	1.196
26	1.246	3.438	1.963	0.548	63.487	1.288	101	1.116	6.411	2.200	0.379	42.352	1.140
27	1.034	5.143	2.715	0.307	32.151	1.057	102	1.018	4.405	2.583	0.578	67.225	1.276
28	0.566	5.997	2.359	0.218	22.234	1.040	103	1.403	6.447	3.081	0.443	50.354	1.249
29	1.082	4.128	2.422	0.280	28.750	1.100	104	1.144	6.590	1.844	0.458	52.246	1.237
30	1.200	5.514	2.800	0.290	31.294	1.126	105	0.974	5.680	2.595	0.568	66.053	1.263
31	1.410	6.429	2.182	0.213	21.612	1.102	106	0.794	4.540	3.393	0.598	69.783	1.253
32	0.570	6.648	3.177	0.451	51.336	1.272	107	0.934	3.918	2.375	0.353	39.122	0.989
33	0.729	6.146	3.125	0.410	46.311	1.243	108	0.913	6.988	2.048	0.517	59.567	1.262
34	1.180	3.709	2.145	0.459	52.414	1.270	109	0.614	5.727	3.330	0.364	40.449	1.112
35	1.125	5.697	3.099	0.386	43.189	1.126	110	0.991	6.091	1.891	0.453	51.674	1.258
36	1.054	5.963	1.523	0.314	32.953	0.979	111	1.216	6.547	3.493	0.214	21.766	1.071
37	0.665	3.032	3.192	0.408	45.983	1.172	112	0.986	4.856	2.819	0.466	53.215	1.231
38	1.455	5.572	2.443	0.560	65.011	1.274	113	0.830	3.992	2.523	0.310	33.753	1.027
39	1.485	6.875	1.715	0.506	58.257	1.259	114	0.898	4.935	2.080	0.266	28.235	0.927
40	0.805	3.169	2.560	0.394	44.204	1.098	115	1.156	3.112	1.733	0.292	31.510	0.971
41	0.559	3.752	1.803	0.552	63.951	1.280	116	1.338	3.787	1.759	0.585	68.081	1.235
42	1.420	6.783	3.322	0.558	64.806	1.277	117	1.189	5.252	2.934	0.524	60.486	1.270
43	0.946	3.582	2.853	0.367	40.856	1.124	118	0.648	4.573	2.228	0.486	55.731	1.261
44	0.715	4.155	1.783	0.325	35.632	1.035	119	0.634	6.104	2.266	0.592	68.950	1.274

**Table 9.** Experiment samples calculated by CFD

No.	$a(mm)$	$b(mm)$	$c(mm)$	$d(mm)$	$\theta(^{\circ})$	$\tau$ (MPa)	Index	$a(mm)$	$b(mm)$	$c(mm)$	$d(mm)$	$\theta(^{\circ})$	$\tau$ (MPa)
45	0.818	5.844	1.937	0.328	35.998	1.075	120	0.603	6.327	2.325	0.474	54.266	1.206
46	1.369	3.677	2.465	0.287	30.869	0.997	121	0.769	5.355	3.163	0.254	26.745	1.208
47	1.462	4.791	2.087	0.267	28.373	0.944	122	0.545	5.386	2.631	0.402	45.234	1.148
48	0.599	5.126	2.673	0.338	37.236	1.081	123	0.686	5.555	1.851	0.377	42.168	1.093
49	1.430	4.710	1.707	0.308	33.438	1.085	124	1.453	5.404	1.653	0.374	41.790	1.058
50	1.091	5.001	2.960	0.593	69.087	1.293	125	0.696	4.971	2.019	0.572	66.525	1.282
51	1.259	3.548	2.115	0.390	43.699	1.060	126	0.963	4.299	1.642	0.426	48.269	1.191
52	1.383	3.231	1.818	0.470	53.760	1.218	127	1.180	6.268	1.875	0.240	24.977	0.990
53	0.584	6.862	2.044	0.236	24.452	0.940	128	0.996	6.185	1.912	0.584	67.964	1.237
54	1.400	3.325	3.448	0.361	40.108	1.145	129	1.051	4.090	2.128	0.436	49.521	1.167
55	0.746	4.258	1.916	0.241	25.089	0.991	130	1.200	3.637	2.637	0.519	59.870	1.255
56	0.724	6.208	3.285	0.347	38.367	1.143	131	1.442	3.906	2.951	0.423	47.916	1.195
57	0.622	3.367	1.821	0.430	48.689	1.212	132	0.903	3.655	2.488	0.476	54.453	1.251
58	1.028	5.311	2.406	0.540	62.520	1.256	133	1.111	5.339	2.739	0.534	61.784	1.266
59	0.757	6.492	3.362	0.556	64.550	1.267	134	0.548	5.179	2.171	0.260	27.459	0.941
60	1.275	6.916	1.771	0.230	23.690	0.942	135	1.326	4.183	2.104	0.285	30.657	1.026
61	0.610	4.830	3.033	0.413	46.682	1.196	136	1.308	6.340	2.291	0.429	48.584	1.201
62	1.252	3.936	2.675	0.346	38.310	1.170	137	1.477	3.136	2.153	0.246	25.762	1.064
63	1.042	3.516	2.874	0.322	35.219	1.113	138	0.884	4.587	2.339	0.446	50.756	1.247
64	0.504	5.898	1.867	0.504	57.995	1.273	139	0.855	6.603	2.385	0.499	57.371	1.276
65	1.021	3.271	2.257	0.588	68.535	1.279	140	1.160	6.544	1.987	0.228	23.487	0.945
66	0.709	3.420	2.772	0.334	36.798	1.091	141	1.093	3.729	3.309	0.357	39.603	1.098
67	1.064	5.909	2.341	0.400	44.951	1.115	142	1.287	3.807	3.138	0.257	27.076	1.039
68	0.971	4.619	2.025	0.527	60.865	1.268	143	1.390	6.830	3.407	0.300	32.461	1.094
69	1.139	3.863	3.246	0.469	53.641	1.267	144	1.469	5.782	3.141	0.461	52.687	1.227
70	0.749	4.098	2.740	0.294	31.795	1.035	145	1.341	4.066	1.995	0.511	58.836	1.219
71	1.375	5.212	2.709	0.439	49.889	1.215	146	0.532	3.251	2.610	0.332	36.549	1.062
72	1.129	3.457	1.577	0.314	34.305	0.982	147	0.589	5.951	2.548	0.432	49.062	1.186
73	1.360	3.054	2.655	0.222	22.750	1.199	148	0.870	5.450	2.998	0.250	26.226	1.060
74	0.922	3.009	1.603	0.507	58.418	1.212	149	0.632	3.302	3.224	0.277	29.675	1.211
75	1.272	5.070	2.910	0.442	50.256	1.215	150	0.917	3.492	2.246	0.207	20.874	1.121